J. Fluid Mech. (2023), *vol*. 964, A29, doi:10.1017/jfm.2023.359

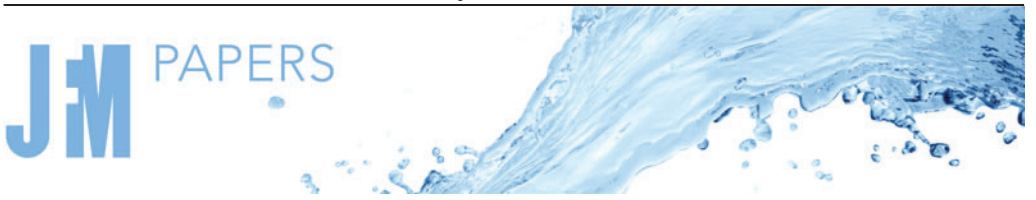

Study of compressible turbulent plane Couette flows via direct numerical simulation

Jie Yao[1] **and Fazle Hussain**[1],†

[1]Department of Mechanical Engineering, Texas Tech University, Lubbock, TX 79409, USA

(Received 25 May 2022; revised 27 February 2023; accepted 17 April 2023)

Compressible turbulent plane Couette flows are studied via direct numerical simulation for wall Reynolds numbers up to $Re_w = 10\,000$ and wall Mach numbers up to $M_w = 5$. Various turbulence statistics are compared with their incompressible counterparts at comparable semilocal Reynolds numbers $Re^*_{\tau,c}$. The skin friction coefficient C_f, which decreases with Re_w, only weakly depends on M_w. On the other hand, the thermodynamic properties (mean temperature, density and others) strongly vary with M_w. Under proper scaling transformations, the mean velocity profiles for the compressible and incompressible cases collapse well and show a logarithmic region with the Kármán constant $\kappa = 0.41$. Compared with wall units, the semilocal units yield a better collapse for the profiles of the Reynolds stresses. While the wall-normal and spanwise Reynolds stress components slightly decrease in the near-wall region, the inner peak of the streamwise component notably increases with increasing M_w – indicating that flow becomes more anisotropic when compressible. In addition, the near-wall turbulence production decreases as M_w increases – due to rapid wall-normal changes of viscosity caused by viscous heating. The streamwise and spanwise energy spectra show that the length scale of near-wall coherent structures does not vary with M_w in semilocal units. Consistent with those in incompressible flows, the superstructures (the large-scale streamwise rollers) with a typical spanwise scale of $\lambda_z/h \approx 1.5\pi$ become stronger with increasing Re_w. For the highest Re_w studied, they contribute about 40 % of the Reynolds shear stress at the channel centre. Interestingly, flow visualization and correlation analysis show that the streamwise coherence of these structures degrades with increasing M_w. In addition, at comparable $Re^*_{\tau,c}$, the amplitude modulation of these structures on the near-wall small scales is quite similar between incompressible and compressible cases – but much stronger than that in plane Poiseuille flows.

Key words: compressible boundary layers, compressible turbulence, turbulence simulation

† Email address for correspondence: fazlehussain@gmail.com

1. Introduction

Plane Couette (PC) flow, the fluid motion between two parallel flat plates moving at different speeds, is one of the simplest canonical configurations for the numerical study of wall turbulence – its statistics and dynamics. In contrast to the extensive study of plane Poiseuille (PP) flows (e.g. Kim, Moin & Moser 1987; Lee & Moser 2015; Hoyas *et al.* 2022), much less attention has been paid to the PC flow. One of the main reasons is that PC flow contains large-scale structures (streamwise-oriented rollers), distributed in counter-rotating pairs across the spanwise domain whose resolution requires an extended computational domain in both the streamwise and spanwise directions. The first direct numerical simulation (DNS) of turbulent PC flows was conducted by Lee & Kim (1991) at the friction Reynolds number $Re_\tau = 170$ with lengths $4\pi h \times 8\pi/3h$ in the streamwise and spanwise directions. Here, h denotes half-channel-height. They found that the most energetic motion at the channel centre occurs at wavenumber $k_x h = 0$ and $k_z h = 1.5$. Later, Komminaho, Lundbladh & Johansson (1996) and Tsukahara, Kawamura & Shingai (2006), respectively, performed DNS at $Re_\tau = 52$ and $Re_\tau = 126$ with a relatively large domain (i.e. $28\pi h \times 8\pi h$ for the former and $64h \times 6h$ for the latter). Avsarkisov *et al.* (2014) conducted DNS at Re_τ up to 550 and showed that the mean velocity profile exhibits a logarithmic region with a slope of 0.41. DNSs for Re_τ up to 986 by Pirozzoli, Bernardini & Orlandi (2014) showed a secondary outer peak in the streamwise turbulent intensity at the highest Re_τ – related to the presence of the large-scale rollers of spanwise wavelength $\lambda_z \approx 5h$. Despite these prior studies, the characteristics of these large-scale motions remain elusive. Lee & Moser (2018) performed DNS with a very large computational domain (*viz.* $100\pi h \times 5\pi h$) for Re_τ up to 500. They found that as Re_τ increases, the large-scale structures become more coherent in the streamwise direction. Recently, Cheng, Pullin & Samtaney (2022) performed wall-resolved as well as wall-modelled large-eddy simulation (LES) of PC flows at Re_τ up to 2600 and 2.8×10^5, respectively. Interestingly, the energy of the large-scale streamwise rollers was found to decrease with increasing Re_τ.

Even fewer studies have targeted the compressible PC flow – most focusing on the linear stability analysis (Chagelishvili, Rogava & Segal 1994; Duck, Erlebacher & Hussaini 1994; Hu & Zhong 1998; Ramachandran *et al.* 2016). For example, Duck *et al.* (1994) showed that, unlike the incompressible equivalent, linear unstable modes exist in compressible PC flow. Malik, Dey & Alam (2008) investigated the linear stability and the non-modal transient growth for both the uniform shear flow with constant viscosity and the non-uniform shear flow with stratified viscosity. They found that both mean flows are linearly unstable for a range of supersonic Mach numbers. Using the resolvent analysis, Dawson & McKeon (2019) studied how the shape and amplitude of the optimal disturbances depend on the Mach number in compressible laminar PC flow.

Regarding DNS of compressible PC flow, the first study was performed by Buell (1991) at bulk Reynolds number $Re_b = 3000$ and bulk Mach number M_b up to 3. He found that the large-scale streamwise rollers become less organized at higher M_b. Szemberg O'Connor's (2018) DNS of compressible PC at two different bulk-to-shear viscosity ratios showed that the bulk (dilatational or second) viscosity has a minor effect on mean flow quantities. To derive an eddy conductivity closure for wall-modelled LES of high-speed flows, Chen *et al.* (2022) recently performed DNS of compressible PC flow with different wall temperatures for wall Mach numbers M_w up to 6.

The present work aims to systematically examine the compressibility effect on PC flow, mainly focusing on how Reynolds and Mach numbers affect turbulence statistics and structures. The remaining paper is organized as follows. Section 2 presents the simulation

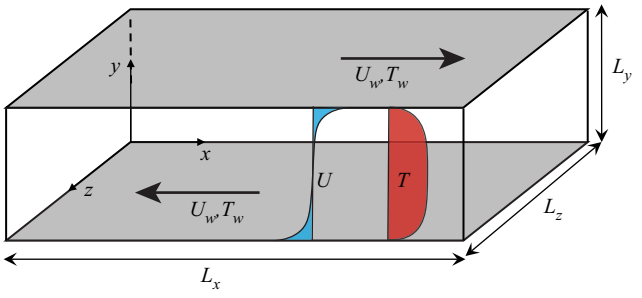

Figure 1. Schematic of the compressible PC flow; x, y and z are the streamwise, wall-normal and spanwise coordinates, with corresponding velocities u, v and w; U_w and T_w denote the wall velocity and temperature.

methods and parameters. Section 3 discusses the main results, including turbulence statistics and structures. Conclusions are drawn in § 4.

2. Numerical set-up

2.1. *Numerical method*

The DNS of the compressible Navier–Stokes equation for the PC flow (figure 1) is conducted with our in-house code (Yao & Hussain 2020). The fluid considered is a perfect gas governed by Sutherland's viscosity law. The seventh-order upwind-biased and eighth-order centred schemes are used for the convective and viscous terms, respectively (Li *et al.* 2010). The low-storage third-order Runge–Kutta algorithm is utilized for time integration. See Yao & Hussain (2020) for more details on the governing equations and the simulation methods. The DNS is conducted in a truncated rectangular box with the dimensions L_x, L_y, L_z in the streamwise (x), wall-normal (y) and spanwise (z) directions. Periodic boundary conditions are specified in the wall-parallel (x, z) directions with constant mesh size, and a mapping function is used in the wall-normal direction. The top and bottom walls move in the streamwise direction with equal and opposite speeds $\pm U_w$, and the isothermal boundary condition is employed for the temperature at the walls T_w. The solver has been extensively validated in our previous works (Yao & Hussain 2019, 2020) for PP configuration. In Appendix A, the code is further validated by comparing a low Mach number PC flow with the strictly incompressible dataset of Lee & Moser (2018).

2.2. *Simulation parameters*

Details on the parameters of the DNS are provided in table 1. In particular, DNS is performed at three wall Reynolds numbers (namely, $Re_w \equiv \rho_b U_w h/\mu_w = 1500$, 4000 and 10 000), where ρ_b is the bulk density, and μ_w is the dynamic viscosity at the wall. For all these Reynolds numbers, two different wall Mach numbers (subsonic $M_w \equiv U_w/c_w = 0.8$ and supersonic 1.5) are considered. Here, c_w represents the speed of sound at the wall temperature. In addition, two higher Mach number (i.e. $M_w = 3$ and 5) cases are considered for $Re_w = 4000$. The computational domain is $L_x \times L_y \times L_z = 24\pi h \times 2h \times 6\pi h$, which, based on the study by Lee & Moser (2018), can yield reasonably good flow statistics. The effect of domain size on flow physics is further examined for the $Re_w = 4000$ and $M_w = 1.5$ case in Appendix B. Both the standard Reynolds (represented by $\bar{\phi}$) and the density-weighted Favre averaging ($\tilde{\phi} = \overline{\rho\phi}/\bar{\rho}$) are used in this study, with ϕ' and ϕ'' denoting their remaining fluctuations. Hereinafter, quantities non-dimensionalized

Case	Re_w	Re_τ	$Re^*_{\tau,c}$	M_w	$N_x \times N_y \times N_z$	Δx^+	Δy^+	Δz^+	Tu_τ/h
C2KM08	1500	96.4	86.0	0.8	$768 \times 129 \times 384$	9.5	0.22–3.15	4.7	47.6
C4KM08	4000	228.4	202.3	0.8	$1536 \times 193 \times 768$	11.2	0.36–4.93	5.6	34.8
C10KM08	10 000	515.9	456.4	0.8	$3072 \times 257 \times 1536$	12.6	0.60–8.36	6.3	29.1
C2KM15	1500	104.9	72.6	1.5	$768 \times 129 \times 384$	10.3	0.25–3.40	5.1	44.2
C4KM15	4000	251.5	172.2	1.5	$1536 \times 193 \times 768$	12.3	0.39–5.44	6.2	33.2
C10KM15	10 000	571.4	389.8	1.5	$3072 \times 257 \times 1536$	14.0	0.66–9.26	7.0	28.2
C4KM30	4000	327.2	113.7	3.0	$1536 \times 193 \times 768$	16.0	0.51–7.07	8.0	30.9
C4KM50	4000	464.2	74.3	5.0	$2048 \times 193 \times 1024$	17.0	0.72–10.02	8.5	25.4

Table 1. Summary of the simulation parameters. The computational domain is $L_x \times L_y \times L_z = 24\pi h \times 2h \times 6\pi h$ for all cases, with h the half-channel height, and Tu_τ/h the total simulation time without transition. Quantities with superscript + are non-dimensionalized with the wall units.

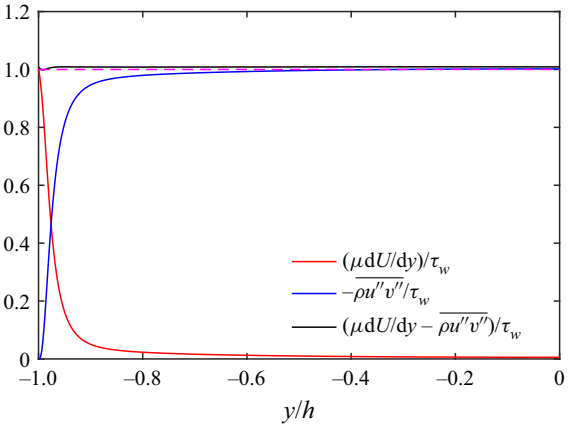

Figure 2. Viscous and turbulent momentum fluxes as a function of y/h for the C10KM15 case.

with semilocal wall units based on the local density and viscosity are represented by the superscript $*$ (i.e. $u^*_\tau = \sqrt{\tau_w/\bar{\rho}}$, $\delta^*_v = \bar{\nu}/u^*_\tau$). Thus, the semilocal Reynolds number is defined as $Re^*_\tau = h/\delta^*_v = Re_\tau\sqrt{(\bar{\rho}/\bar{\rho}_w)}/(\bar{\mu}/\bar{\mu}_w)$.

The convergence of our DNSs is checked by examining the mean momentum equation, which is given as

$$\mu dU/dy - \overline{\rho u'' v''} = \tau_w. \tag{2.1}$$

Figure 2 shows the viscous, turbulent momentum fluxes and their sum for the C10KM15 case. Results of other cases, which are quite similar, are not shown here for brevity. For all cases, the maximum error in the total flux is within 2 % and is comparable to prior DNS studies (Szemberg O'Connor 2018; Chen *et al.* 2022).

The incompressible DNS data for the smaller domain size (i.e. $20\pi h \times 5\pi h$) by Lee & Moser (2018) at $Re_\tau = 93$ (ILM93), 220 (ILM200) and 500 (ILM500) are employed for comparison.

In addition, for better comparison, four additional DNSs at similar $Re^*_{\tau,c} \equiv Re_\tau\sqrt{\bar{\rho}_c/\bar{\rho}_w}/(\bar{\mu}_c/\bar{\mu}_w)$ as C2KM15, C4KM15, C4KM30 and C10KM15 cases are performed using the same code as Lee & Moser (2018). Details of these incompressible simulation parameters (e.g. domain sizes and grid resolutions) are listed in table 2.

Case	Re_w	Re_τ	$N_x \times N_y \times N_z$	Δx^+	Δy^+	Δz^+	Tu_τ/h
I1KM00	1176	75	$512 \times 128 \times 256$	11.0	0.04–1.8	5.5	59.6
I2KM00	1852	112	$768 \times 128 \times 384$	11.0	0.06–2.6	5.5	54.9
I3KM00	3030	172	$1024 \times 128 \times 512$	12.7	0.1–4.0	6.3	51.3
I8KM00	7519	384	$2048 \times 192 \times 1024$	14.1	0.14–5.9	7.1	45.7

Table 2. Summary of the parameters used for the strictly incompressible PC flow. The simulation domain is $24\pi h \times 2h \times 6\pi h$.

Case	Re_w	Re_τ	M_w	$\bar{\rho}_w/\rho_b$	$\bar{\rho}_c/\rho_b$	$\bar{T}_c/T_w$	$10^2 M_{\tau w}$	$10^3 C_f$	$-10^2 B_q$	$\mu(y_P^*)/\mu_w$	$P_k^+(y_P^*)$
C2KM08	1500	96.4	0.8	1.09	0.99	1.09	4.73	7.60	1.46	1.056	0.236
C4KM08	4000	228.4	0.8	1.10	0.99	1.10	3.76	5.95	1.32	1.052	0.238
C10KM08	10 000	515.9	0.8	1.10	0.99	1.10	7.07	4.84	1.18	1.049	0.239
C2KM15	1500	104.9	1.5	1.31	0.97	1.34	4.17	7.47	4.74	1.189	0.211
C4KM15	4000	251.5	1.5	1.33	0.98	1.35	8.02	5.92	4.19	1.182	0.213
C10KM15	10 000	571.4	1.5	1.35	0.98	1.36	6.36	4.84	3.75	1.171	0.216
C4KM30	4000	327.2	3.0	2.29	0.93	2.39	10.70	5.82	12.71	1.648	0.157
C4KM50	4000	464.2	5.0	4.56	0.92	4.83	12.72	5.90	25.23	2.521	0.114

Table 3. DNS results for some global parameters: the wall and centreline normalized densities ($\bar{\rho}_w/\rho_b$ and $\bar{\rho}_c/\rho_b$); the centreline temperature ($\bar{T}_c/T_w$); the friction Mach number ($M_{\tau w} = u_\tau/\bar{c}_w$); the skin friction coefficient ($C_f = 2\tau_w/(\rho_b U_w^2)$); the heat flux at the wall ($B_q = \bar{q}_w/(c_p\bar{\rho}_w u_\tau T_w)$); and the viscosity at the location of peak turbulent kinetic energy production ($\mu(y_P^*)/\mu_w$).

3. Results

3.1. *Skin friction and heat flux*

Table 3 enumerates some characteristic quantities, including the mean densities at the wall ($\bar{\rho}_w$) and channel centreline ($\bar{\rho}_c$), the temperature at the centreline ($\bar{T}_c$), skin friction (C_f) and heat flux (B_q) coefficients, etc.

The skin friction coefficient C_f decreases with increasing Re_τ, as expected. For incompressible cases, Robertson & Johnson (1970) suggested the empirical correlation for C_f

$$\sqrt{\frac{C_f}{2}} = \frac{G}{\log Re_w}, \tag{3.1}$$

where constant G is chosen to fit the DNS results. Various choices for G in the range of $0.18 - 0.21$ were proposed (El Telbany & Reynolds 1982; Kitoh, Nakabayashi & Nishimura 2005; Tsukahara *et al.* 2006; Pirozzoli *et al.* 2014).

Figure 3 compares the present DNS data with (3.1), together with several incompressible data available in the literature. The difference in C_f among different M_w cases is minor, and all closely follow the prediction based on (3.1) with $G = 0.21$.

As in the compressible PP flows (Yao & Hussain 2020), the magnitude of wall heat flux B_q for a given M_w decreases with increasing Re_w. The Reynolds-averaged energy equation is given as

$$\frac{\partial\overline{(e+p)v}}{\partial y} = \frac{\partial\overline{u\sigma_{xy}}}{\partial y} + \frac{\partial\overline{v\sigma_{yy}}}{\partial y} + \frac{\partial\overline{w\sigma_{yz}}}{\partial y} + \frac{\partial}{\partial y}\left(k\frac{\partial\bar{T}}{\partial y}\right), \tag{3.2}$$

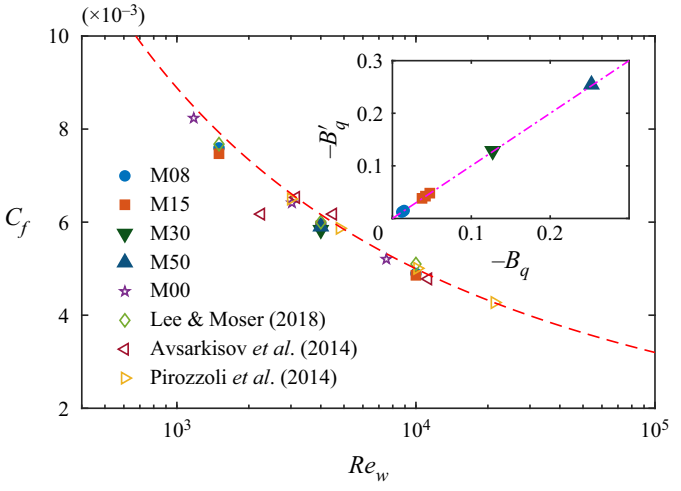

Figure 3. Skin friction coefficient (C_f) as a function of Re_w. The dashed line represents the friction law (3.1) with $G = 0.21$, and the inset shows the correlation between B_q and $B'_q = -(M_c^2(\gamma - 1)/(2\rho_w u_\tau)/(\rho_b U_b))C_f$ with the dash-dotted line denoting $B_q = B'_q$.

where $e = \rho(e_s + u_i u_i/2)$ is the total energy per unit mass – equal to the sum of internal (e_s) and kinetic energies; σ_{ij} the viscous stress tensor and $k = c_p\mu/Pr$ is the thermal conductivity, with c_p the specific heat at constant pressure and Pr the Prandtl number.

By integrating (3.2) from the wall surface to the channel centreline, one obtains

$$q_w \left(\equiv -k \left. \frac{\partial \bar{T}}{\partial y} \right|_w \right) = -U_w \tau_w. \tag{3.3}$$

Then, similar to that obtained by Huang, Coleman & Bradshaw (1995) and Li *et al.* (2019) for the compressible PP flows, we have the following correlation between B_q and C_f for PC:

$$B_q = -\frac{M_w^2(\gamma - 1)}{(2\rho_w u_\tau)/(\rho_b U_w)} C_f, \tag{3.4}$$

where $\gamma (= 1.4)$ is the specific heat ratio.

The inset in figure 3 shows that all DNS results agree well with the proposed correlation (3.4). Similar to the decomposition for C_f (e.g. Fukagata, Iwamoto & Kasagi 2002; Renard & Deck 2016), (3.4) enables us to evaluate B_q based on the statistical quantities away from the wall, which can be more accurately obtained than temperature gradient at the wall.

3.2. *Mean velocity profiles*

In the presence of compressibility, the van Driest (VD) transformation (Driest 1951)

$$U_D^+(y) = \int_0^{U^+} \sqrt{\frac{\bar{\rho}}{\bar{\rho}_w}}\, \mathrm{d}U^+, \tag{3.5}$$

is typically employed to transform the mean velocity profiles to an equivalent incompressible case. Although VD transformation works well for compressible flows over adiabatic walls (Duan, Beekman & Martin 2010; Pirozzoli & Bernardini 2011;

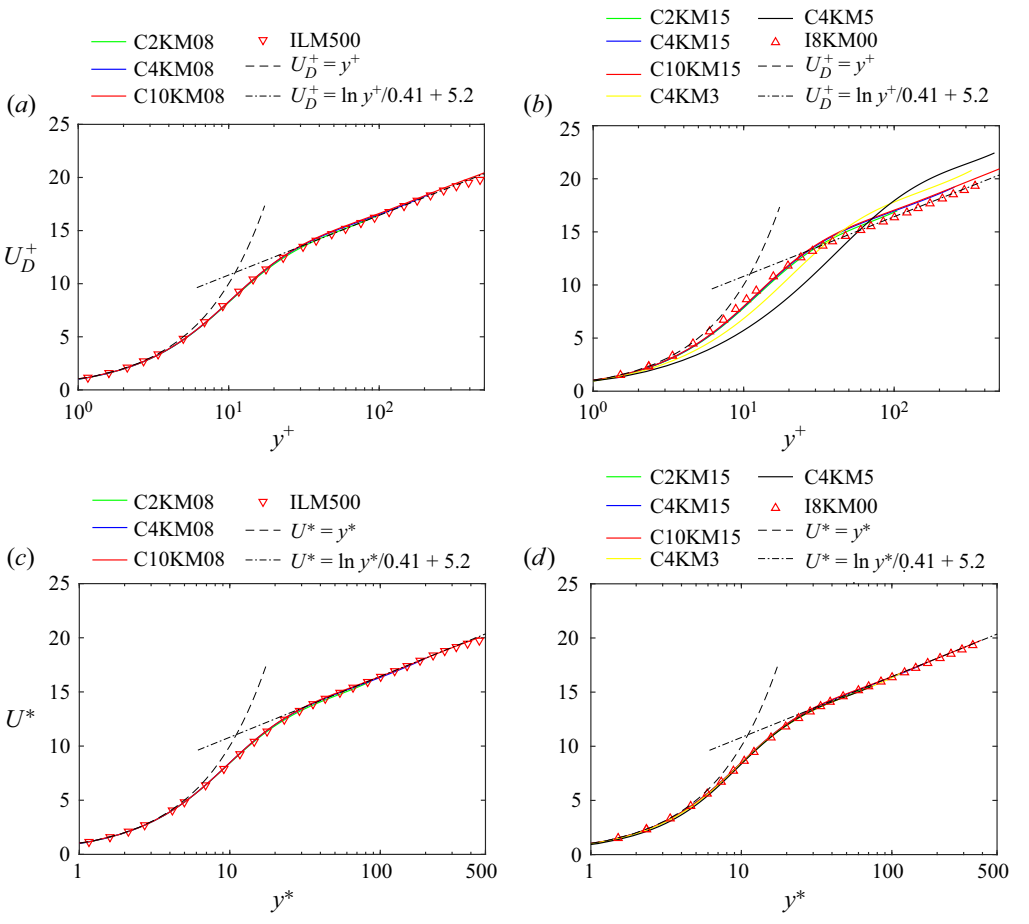

Figure 4. Mean velocity profiles using (*a*,*b*) the VD and (*c*,*d*) TL transformations for subsonic (i.e. $M_w = 0.8$) (*a*,*c*) and supersonic (i.e. $M_w = 1.5$, 3 and 5) (*b*,*d*) cases.

Hadjadj *et al.* 2015), its performance deteriorates for flows over diabatic walls (Duan *et al.* 2010). Figures 4(*a*) and 4(*b*) display the VD transformed mean velocity profiles for subsonic (i.e. $M_w = 0.8$) and supersonic (i.e. $M_w = 1.5$, 3 and 5) cases, respectively. The incompressible cases ILM500 and I8KM00 are also included for comparison in (a) and (b), respectively. For subsonic ($M_w = 0.8$) cases, the VD transformation yields good collapses between different cases; for supersonic (particularly Re4KM50) cases, it undershoots and overshoots the incompressible profile in the viscous and log layer, respectively – consistent with the previous findings for the compressible PP (Modesti & Pirozzoli 2016; Patel, Boersma & Pecnik 2016; Yao & Hussain 2020) and boundary layer (Duan *et al.* 2010; Zhang, Duan & Choudhari 2018) flows.

To incorporate the non-zero wall heat flux effect, Trettel & Larsson (2016) derived a velocity transformation based on the log law and stress-balance conditions

$$U^*(y) = \int_0^{U^+} \sqrt{\frac{\bar{\rho}}{\bar{\rho}_w}} \left[1 + \frac{1}{2\bar{\rho}}\frac{\mathrm{d}\bar{\rho}}{\mathrm{d}y}y - \frac{1}{\bar{\mu}}\frac{\mathrm{d}\bar{\mu}}{\mathrm{d}y}y\right] \mathrm{d}U^+. \tag{3.6}$$

The Trettlel & Larsson (TL) transformation, which is equivalent to Patel *et al.* (2016), includes not only the change of density but also the relative change of density and

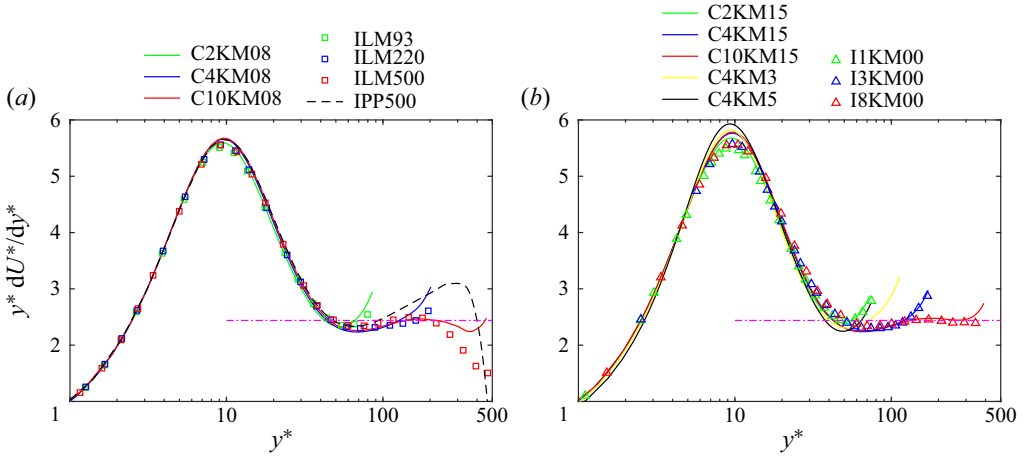

Figure 5. The log-law diagnostic function of the TL transformed velocities $\beta = y^*(\mathrm{d}U^*/\mathrm{d}y^*)$ for (*a*) subsonic and (*b*) supersonic cases. Note that the IPP500 case in (*a*) is for incompressible PP flow at $Re_\tau = 500$ (Yao, Chen & Hussain 2019), and the dash-dotted line represents $\beta = 1/\kappa$ with $\kappa = 0.41$.

viscosity gradient across the channel. It was demonstrated to be able to collapse mean velocity profiles for compressible PP flows (Modesti & Pirozzoli 2016; Yao & Hussain 2020) and also for non-adiabatic turbulent boundary layers (Zhang *et al.* 2018). Recently, Griffin, Fu & Moin (2021) proposed a transformation by accounting for the distinct effects of compressibility on the viscous and turbulent shear stresses. This yielded comparable results to the TL transformation for internal (channel and pipe) flows, and better collapse of the velocity profile for heated, cooled and adiabatic boundary layer flows.

Figure 4(*c*,*d*) shows the mean velocity profiles based on the TL transformation as a function of $y^*(= yRe_\tau^*)$ for subsonic and supersonic cases. Apparently, this overcomes the limitation of the VD transformation. As in PP flows (Modesti & Pirozzoli 2016; Patel *et al.* 2016), a nearly perfect collapse occurs across the whole wall-normal range between the incompressible case and the transformed mean velocity U^* for all M_w cases. Different from the PP flow (Yao & Hussain 2020), where the U^* profiles at low Re_τ typically lie above those at high Re_τ due to the wake effect, U^* for PC flows agree well with each other for all Re_τ – even near the channel centre.

To further examine the logarithmic region, figure 5 shows the corresponding diagnostic function $\beta = y^*(\mathrm{d}U^*/\mathrm{d}y^*)$ for the mean velocity profile under TL transformation. As the Reynolds number increases, the β profiles collapse for y^* up to 50, and slowly develop a plateau with $\beta = 1/\kappa = 1/0.41$ – larger than those reported for other types of wall turbulence (Lee & Moser 2015; Pirozzoli *et al.* 2021; Yao, Chen & Hussain 2022). In addition, at a common $Re_{\tau,c}^*$ (e.g. figure 5*b*), the compressible and incompressible cases agree very well. Notable differences appear between PC and PP flows (figure 5*a*) – akin to that found in incompressible flow by Avsarkisov *et al.* (2014). In particular, for the Re_τ considered, β in PC flow is much flatter than that in PP flow, which indicates that the log layer in the former is less sensitive to the Reynolds number effect. For the ILM500 case (figure 5*a*), β starts to drop sharply at $y^* = 200$. Such a drop, also observed for even higher Re_τ DNS (Pirozzoli *et al.* 2014) and LES (Chen *et al.* 2022) studies, is not apparent for the compressible cases considered here – presumably due to relatively low $Re_{\tau,c}^*$.

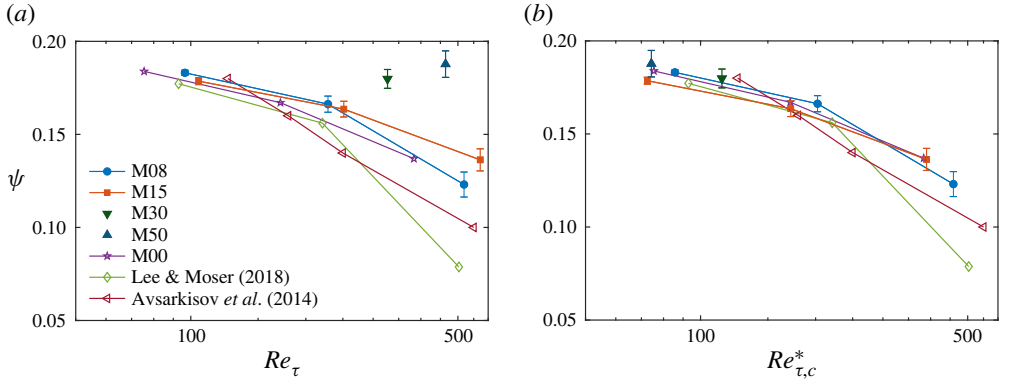

Figure 6. Mean velocity gradient at the channel centreline ψ and its uncertainty as functions of (*a*) Re_τ and (*b*) $Re^*_{\tau,c}$.

Another important question in PC flows is the Reynolds number dependence of the velocity gradient at the channel centreline, which is defined as

$$\psi = \frac{h}{U_w}\frac{\mathrm{d}U}{\mathrm{d}y}\bigg|_{y/h=0}. \tag{3.7}$$

In PP flows, ψ is always zero by symmetry, but in PC flow, ψ is not necessarily zero as the mean velocity becomes anti-symmetric. As ψ is directly related to turbulence production in the outer region, understanding its behaviour with increasing Reynolds number is essential and has been debated in many incompressible works. For example, based on the experimental results by Reichardt (1959), Busse (1970) suggested that ψ approaches 0.25 at infinite Reynolds number. However, Lund & Bush (1980) performed an asymptotic analysis and suggested that ψ should approach zero as $Re \to \infty$. Recently, Chen *et al.* (2022) proposed that ψ should decrease exponentially for sufficiently high Reynolds numbers.

Figure 6(*a*) shows the Re_τ dependence of ψ for different M_w cases, along with the incompressible results of Lee & Moser (2018) and Avsarkisov *et al.* (2014). The uncertainty of ψ due to averaging over limited time samples is estimated via an autoregressive method as described in Oliver *et al.* (2014) and Rezaeiravesh *et al.* (2022). Consistent with previous findings, at a given M_w, ψ decreases with Re_τ, but the Reynolds number range considered is too narrow to predict the asymptotic behaviour of ψ. There is a notable scatter among different M_w cases, particularly at large Re_τ, and the discrepancy is beyond the uncertainty limit. However, such scatter can be significantly reduced by plotting ψ as a function of $Re^*_{\tau,c}$ (figure 6*b*), in which reasonably good collapses can be observed between different M_w cases. It suggests that the scaling of ψ should follow the incompressible situation when local flow properties are taken into consideration. The larger discrepancy for the incompressible cases among different datasets might be attributed to the domain size effect. For example, Lee & Moser (2018) found approximately 14 % variation in ψ between their small and large domain cases. This is further supported by the results in Appendix B, where ψ between different domain sizes varies about 16 % for $Re_w = 4000$ and $M_w = 1.5$ case.

3.3. *Reynolds stresses*

The non-zero Reynolds stresses $\tau_{ij} = \bar{\rho} R_{ij}$ with $R_{ij} = \widetilde{u_i'' u_j''} = \widetilde{u_i u_j} - \widetilde{u}_i \widetilde{u}_j$ are examined here. Figure 7 shows the normalized Reynolds normal stresses (τ_{11}/τ_w, τ_{22}/τ_w and τ_{33}/τ_w) for subsonic (left) and supersonic (right) cases. The streamwise Reynolds stress τ_{11}/τ_w increases with Re_τ, presumably resulting from the enhanced outer large-scale structures (Marusic *et al.* 2010). Different from PP flows, τ_{11}/τ_w near the centreline strongly depends on Re_τ – partially due to non-zero turbulence production there. For the ILM500 case, a secondary peak of τ_{11}/τ_w develops at $y^* \approx 200$; but such a peak has not been observed for compressible cases, perhaps due to relatively low $Re^*_{\tau,c}$.

For the subsonic cases, the locations of the inner peaks are similar in the semilocal unit, namely, $y^* \approx 15$ – consistent with other types of wall turbulence, such as PP (Lee & Moser 2015), pipe (Wu, Baltzer & Adrian 2012; Yao *et al.* 2023) and boundary layer (Schlatter & Örlü 2010). However, as M_w increases, the inner peak locations seem to move closer to the wall – becoming approximately 13.6 for $M_w = 5.0$. At comparable $Re^*_{\tau,c}$ (figure 7*b*), τ_{11}/τ_w for the compressible cases agrees with the incompressible cases in the outer region but is larger near the wall – a feature also found for compressible PP flows (Modesti & Pirozzoli 2016; Yao & Hussain 2020; Baranwal, Donzis & Bowersox 2022) and cooled supersonic/hypersonic turbulent boundary layer (Zhang *et al.* 2018).

Figure 8(*a*) further shows the inner peak value of streamwise Reynolds stress (τ^p_{11}/τ_w) as a function of $Re^*_{\tau,c}$. As expected, the τ^p_{11}/τ_w grows with $Re^*_{\tau,c}$ (Lozano-Durán & Jiménez 2014; Lee & Moser 2015; Marusic, Baars & Hutchins 2017). Note that the Reynolds number scaling of τ^p_{11} is still a highly debated issue in incompressible wall turbulent flows. Previously, τ^p_{11}/τ_w was assumed to increase logarithmically with Re_τ (Marusic & Monty 2019). Recently, Chen & Sreenivasan (2021), based on the bounded wall dissipation assumption, argued that the growth of τ^p_{11}/τ_w would eventually saturate at infinite Reynolds number. The limited number and relatively narrow range of Reynolds numbers considered here prohibit us from opining as to which scaling law better fits the data. In addition, different from ψ, τ^p_{11}/τ_w does not collapse among different M_w cases even if the semilocal unit is employed. Similar behaviour has been recently reported in the compressible PP flows (Yao & Hussain 2020) and hypersonic turbulent boundary layers (Zhang *et al.* 2018). As explained by Foysi, Sarkar & Friedrich (2004), the main reason is that due to the non-local effect between the pressure and fluid inertia, the mean density $\bar{\rho}$ does not preserve inner scaling and, hence, cannot yield complete collapse between compressible and incompressible cases.

Different from τ_{11}/τ_w, good agreements are observed for the wall-normal (τ_{22}/τ_w) and spanwise (τ_{33}/τ_w) components between incompressible and compressible cases at matching $Re^*_{\tau,c}$, with the exception of the region immediately adjacent to the wall. This agrees with the previous observations for compressible turbulent PP flows (Modesti & Pirozzoli 2016; Yao & Hussain 2020) and boundary layers (Duan, Beekman & Martin 2011; Huang, Duan & Choudhari 2022). With increasing $Re^*_{\tau,c}$, τ_{33}/τ_w increases, but τ_{22}/τ_w remains nearly unchanged – distinctly different from the PP flows. From figure 8(*b*), it is clear that the inner peak value of spanwise Reynolds stress (τ^p_{33}/τ_w) grows with $Re^*_{\tau,c}$. In addition, in contrast to τ^p_{11}/τ_w, τ^p_{33}/τ_w is independent of M_w.

Figure 9 further shows the Reynolds shear stress (τ_{12}/τ_w). It starts from zero and increases asymptotically to unity at the channel centre. Similar to τ_{22}/τ_w, there is substantial concordance between incompressible and supersonic situations at matching $Re^*_{\tau,c}$, except for the near-wall region. Different from the PP flow, where τ_{12}/τ_w exhibits slow but consistent growth with Reynolds number, τ_{12}/τ_w for PC flows collapses very well

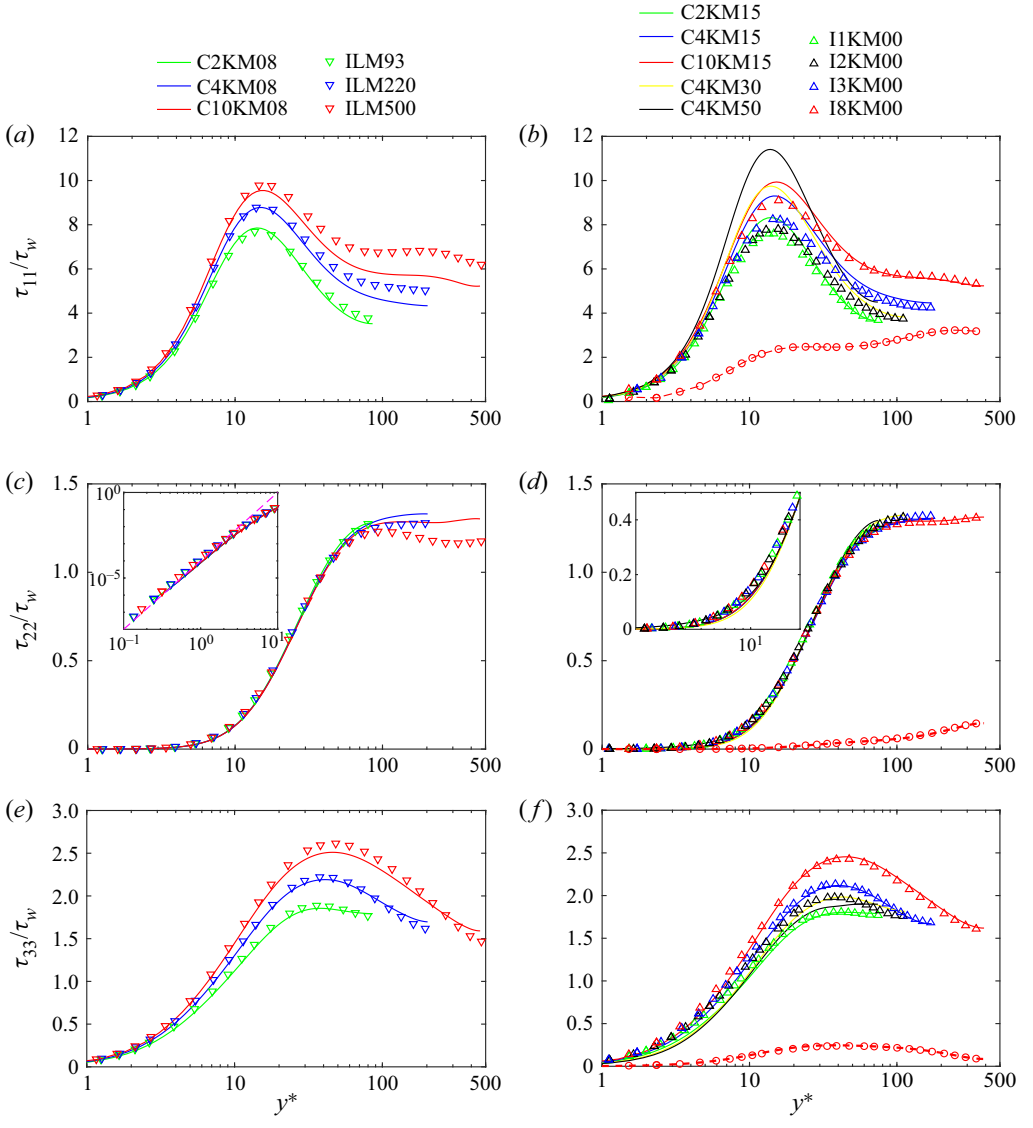

Figure 7. Reynolds normal stress (non-dimensionalized by τ_w) for (*a*,*c*,*e*) subsonic and (*b*,*d*,*f*) supersonic cases: (*a*,*b*) τ_{11}; (*c*,*d*) τ_{22}; (*e*,*f*) τ_{33}. The dashed line in the inset of (*c*) denotes $\tau_{22}/\tau_w = by*^4$ with $b = 1.0 \times 10^{-4}$, and the dashed line (- - - - -, red) and circles (○, red) in (*b*,*d*,*f*) denote the contribution of large-scale structures (with spanwise wavelength $\lambda_z \geq 2h$) to the Reynolds stresses for C10KM15 and I8KM00, respectively.

between different $Re^*_{\tau,c}$ cases – indicating that τ_{12}/τ_w is nearly universal in inner scaling in PC flows.

Recently, Baranwal *et al.* (2022) found that, even if the semilocal scaling is used, the near-wall asymptotic behaviour of Reynolds stresses for compressible PP flow differs from the corresponding incompressible flow. In particular, due to the constraint of the solenoidality of the velocity field, the near-wall asymptotic behaviour exhibits the theoretical behaviour for low Mach numbers flows, e.g. $\tau_{22}/\tau_w \sim y*^4$ (figure 7*c*) and $\tau_{12}/\tau_w \sim y*^3$ (figure 9*a*). However, wall-normal Reynolds stresses and Reynolds shear

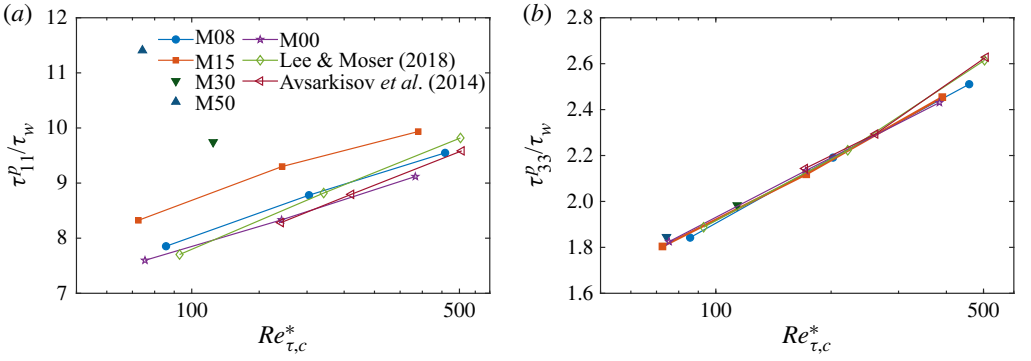

Figure 8. Peak values of (*a*) streamwise τ_{11}/τ_w and (*b*) spanwise τ_{33}/τ_w Reynolds normal stresses as a function of $Re^*_{\tau,c}$.

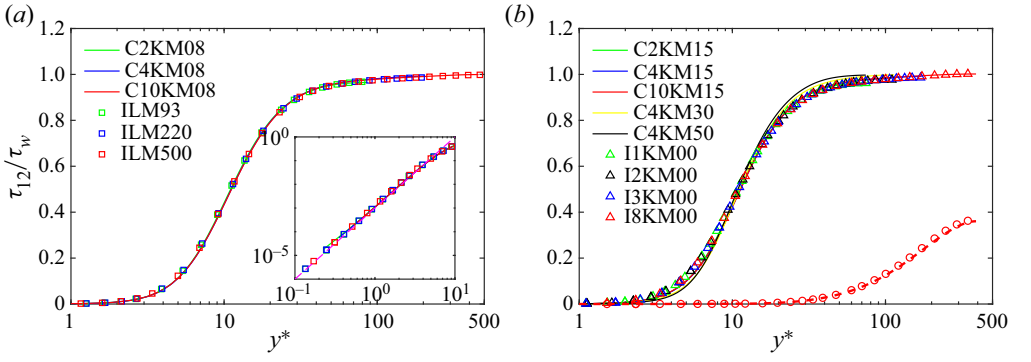

Figure 9. Reynolds shear stress (non-dimensionalized by τ_w) for (*a*) subsonic and (*b*) supersonic cases. The dashed line in the inset of (*a*) denotes $\tau_{12}/\tau_w = cy*^3$ with $b = 1.0 \times 10^{-3}$, and the dashed lines and circles in (*b*) denote the contribution of large-scale structures (with spanwise wavelength $\lambda_z \geq 2h$) for C10KM15 and I8KM00, respectively.

stress components exhibit a decrease in slope as Mach number increases due to increased dilatation effects. This is confirmed in figures 7(*d*) and 9(*b*). Therefore, in the near-wall region, flow in compressible PC becomes more anisotropic than incompressible cases.

The turbulent kinetic energy production $P_k = -\tau_{12}\,\mathrm{d}\tilde{U}/\mathrm{d}y$ normalized by wall variables μ_w/τ_w^2 is displayed in figure 10. As expected, production is mainly concentrated in the near-wall region and well collapses between different Re_w at the same M_w. Different from PP, PC flow has non-zero production at the channel centreline, whose value decreases with increasing Re_w. Assuming $\mathrm{d}\tilde{U}^+/\mathrm{d}y^+ \cong \mathrm{d}U^+/\mathrm{d}y^+$ (as the correlation $\overline{\rho' u'}$ is small), (2.1) gives

$$P_k = -\frac{\mu_w}{\mu}\tau_{12}^+(1+\tau_{12}^+). \tag{3.8}$$

Based on (3.8), the maximum of P_k^+ is approximately equal to 1/4 for the incompressible cases, where $\mu_w/\mu = 1$ – consistent with the results shown in figure 10. In addition, the peak occurs where the Reynolds shear stress $-\tau_{12}^+$ equals the viscous stress $\mathrm{d}\tilde{U}^+/\mathrm{d}y^+$.

From figure 10, the peak production decreases with increasing M_w. However, the peak location y_P^* is roughly the same for all cases in the semilocal coordinates (i.e. $y^* \approx 11$). In addition, τ_{12}^+ collapses well between different M_w cases and is roughly equal to 1/2

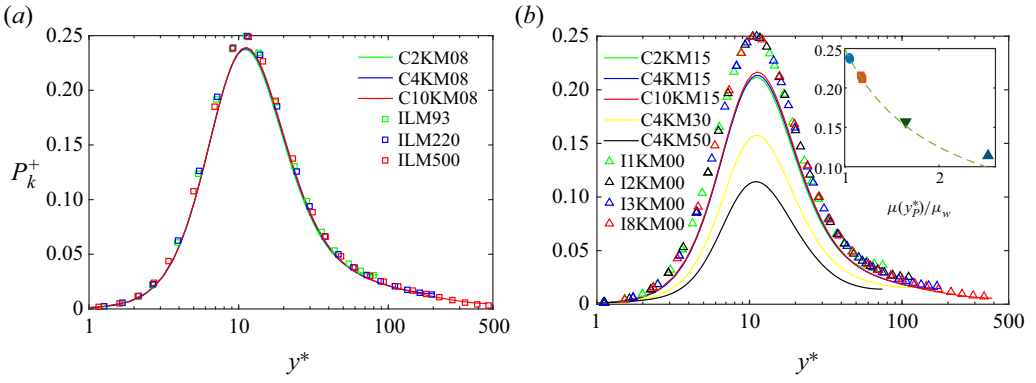

Figure 10. Turbulent kinetic energy production $P_k = -\tau_{12}^+ \mathrm{d}\tilde{U}^+/\mathrm{d}y^+$ as a function of y^* for (*a*) subsonic and (*b*) supersonic cases. The inset in (*b*) displays the peak production $P_k^+(y_P^*)$ as a function of $\mu_w/\mu(y_P^*)$ with the dashed line denoting $P_k^+(y_P^*) = (\mu_w/\mu(y_P^*))/4$.

at $y_P^* \approx 11$(figure 9). Therefore, following (3.8), the peak production for the compressible cases can be estimated as $P_k^+(y_P^*) = (\mu_w/\mu(y_P^*))/4$ – suggesting that the decreases of P_k^+ at high M_w are mainly due to the increase of viscosity. Table 3 lists $\mu(y_P^*)/\mu_w$ for different cases. It is clear that $\mu(y_P^*)/\mu_w$ is less sensitive to Re_w than M_w. In addition, as shown in the inset of figure 10(*b*), the peak production as a function of $\mu(y_P^*)/\mu_w$ closely follows the prediction.

3.4. *Thermodynamic variables*

The mean fluid thermodynamic properties are of great importance in fully developed compressible wall turbulence. Specifically, a key to understanding them lies in the rapid wall-normal changes in $\bar{\rho}$ and $\bar{T}$ due to viscous heating (Ghosh, Foysi & Friedrich 2010). Figure 11(*a*) shows the mean temperature $\bar{T}/T_w$ as a function of y^*. Note that for the current configuration, as the heat transfer at the wall should balance the viscous heating, the temperature at the wall should be lower than that in the flow. As a result, $\bar{T}/T_w$ continuously increases with y^* and becomes roughly constant in the channel centre – consistent with the observation in isothermal compressible PP flows (Huang *et al.* 1995; Yao & Hussain 2020). And the temperature at the centre of the channel $\bar{T}_c$ only weakly depends on Re_τ^*. In particular, $\bar{T}_c/T_w$ is approximately 1.1 for all the subsonic $M_w = 0.8$ cases (table 3). Due to enhanced viscous heating, $\bar{T}/T_w$ increases with M_w notably. For example, $\bar{T}_c/T_w$ increases to 2.39 and 4.84 for $M_w = 3$ and 5, respectively. Correspondingly, the mean density $\bar{\rho}/\rho_w$ has its maximum at the wall and rapidly decreases with increasing y, particularly for the C4KM50 case (figure 11*c*). In addition, $\bar{\rho}/\rho_w$ reaches a plateau near the channel centre – indicating the flow is mostly incompressible in the core. Its value, which only mildly varies with Re_w, progressively decreases with increasing M_w.

Figure 11(*b*) shows $(\bar{T} - T_w)/T_\tau$ as a function of y^*. Here, $T_\tau = q_w/(\rho_w c_p u_\tau) = -B_q T_w$ is the friction temperature. While the agreement between different M_w is improved in the near-wall region, notable differences can be observed, particularly for the $M_w = 5$ case – confirming the previous claim that the mean thermodynamic properties, such as $\bar{\rho}$, $\bar{T}$ and $\bar{\mu}$, do not preserve inner scaling.

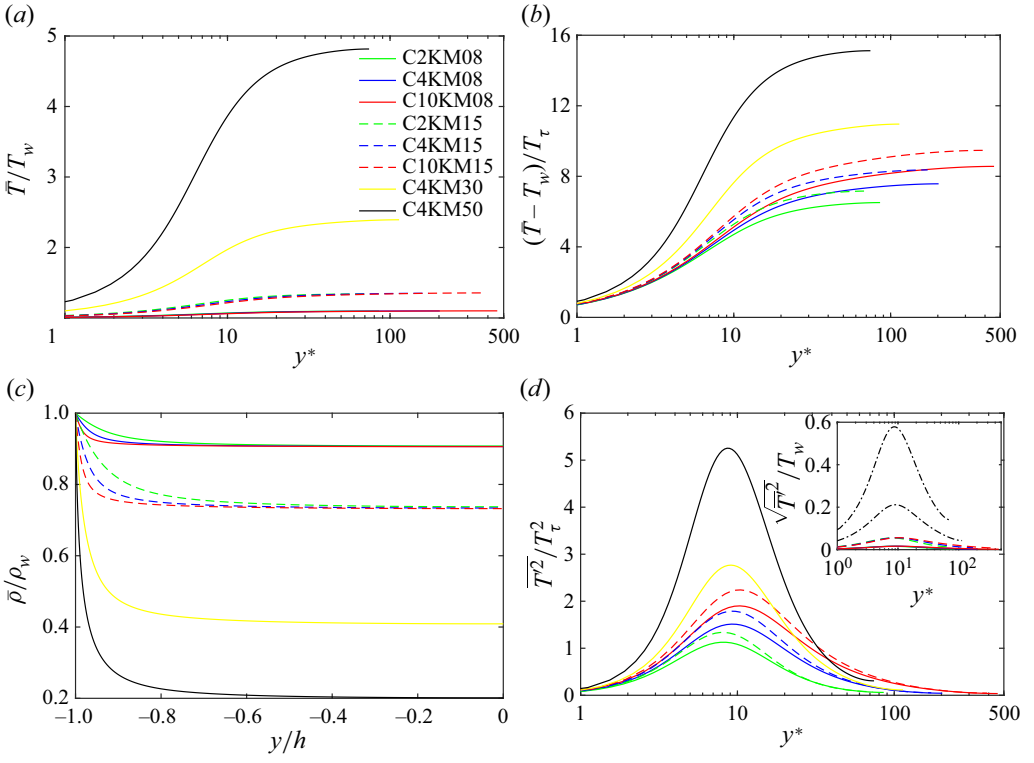

Figure 11. Mean temperature $\bar{T}$ normalized by (*a*) wall temperature T_w and (*b*) friction temperature T_τ as a function of y^*; mean density $\bar{\rho}$ normalized by wall density ρ_w as a function of y/h, and temperature fluctuations $\overline{T'^2}/T_\tau^2$ as a function of y^*. The inset in (*d*) is the root-mean-square (r.m.s.) of the temperature fluctuations normalized by the wall temperature $\sqrt{\overline{T'^2}}/T_w$.

Figure 11(*d*) shows the temperature fluctuations $\overline{T'^2}$ (normalized by T_τ^2) as a function of y^*. For a given Re_w, $\overline{T'^2}/T_\tau^2$ collapses between different M_w in the outer region. Consistent with τ_{11}/τ_w, $\overline{T'^2}/T_\tau^2$ increases with both Re_τ^* and M_w in the near-wall region. In addition, the location of the peak, which remain almost unchanged with M_w, shifts towards large y^* at high Re_τ^*. While the peak value of root-mean-square (r.m.s.) temperature fluctuations $\sqrt{\overline{T'^2}}$ is negligible (within 1 % of T_w) for $M_w = 0.8$ cases, it strongly increases with M_w – becoming approximately 21 % and 57 % for $M_w = 3$ and 5 cases, respectively. This suggests that the fluctuations of thermodynamic properties become progressively important at high M_w.

The mean temperature can be used to determine the mean velocity profiles and the relation between heat transfer and skin friction coefficients. Here, we provide an assessment of various velocity–temperature relationships in compressible PC flows (Walz 1969; Duan *et al.* 2011; Zhang *et al.* 2014), which can be written as

$$\frac{T}{T_w} = 1 + \alpha_1 \frac{U}{U_w} + \alpha_2 \left(\frac{U}{U_w}\right)^2, \tag{3.9}$$

with parameters α_1 and α_2 vary for different scaling relations. Note that different from PP flow, where the centreline velocity is used, U_w is employed here for the

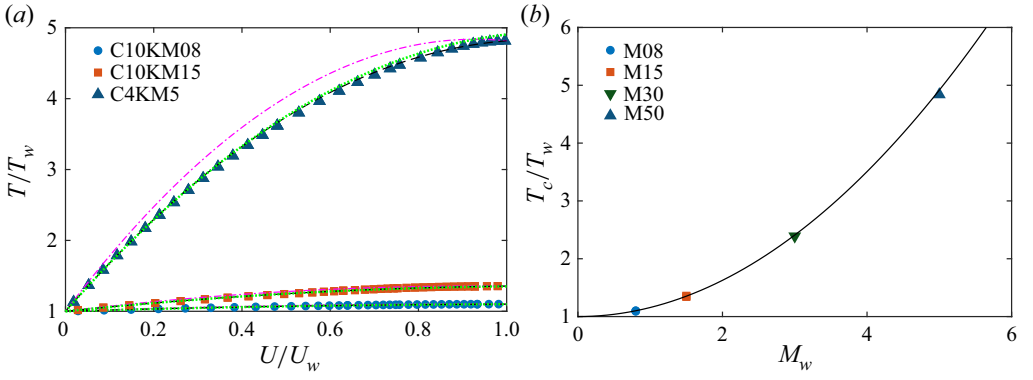

Figure 12. (*a*) Mean temperature (T/T_w) as a function of mean velocity U/U_w for C10KM08, C10KM15 and C4KM50, compared with (3.10*a*,*b*) (dashed-dotted line), (3.11*a*,*b*) (dashed line) and (3.11*a*,*b*) with T_c estimated based on (3.12)(dotted); and (*b*) the temperature at the centreline (T_c/T_w) as a function of M_w and (*b*). Note that the solid line in (*b*) denotes the relation (3.12) with $r_c = 0.783$.

velocity normalization. For the Walz relation,

$$\alpha_1 = \frac{T_r - T_w}{T_w}, \quad \alpha_2 = -r\frac{\gamma - 1}{2}M_c^2\frac{T_c}{T_w U_w^2}. \tag{3.10a,b}$$

Here, $r = Pr^{1/3} = 0.89$ is the recovery factor and $T_r = T_c[1 + (\gamma - 1)rM_c^2/2]$ is the recovery temperature. Similar to the VD transformation for the mean velocity, the Walz relation and DNS are in good agreement for the boundary layer over an adiabatic wall (Pirozzoli, Grasso & Gatski 2004), but have clear differences for diabatic cases (Duan *et al.* 2010).

Zhang *et al.* (2014) later derived a generalized Reynolds analogy

$$\alpha_1 = \frac{T_{rg} - T_w}{T_w}, \quad \alpha_2 = \frac{T_c - T_{rg}}{T_w}, \tag{3.11a,b}$$

with $r_g = 2C_p(T_w - T_c)/U_w^2 - 2Prq_w/(U_w\tau_w)$ the so-called general recovery factor and $T_{rg} = T_c + r_g U_w^2/(2C_p)$.

Figure 12(*a*) compares the DNS data with these velocity–temperature relations. Equation (3.11*a*,*b*) provides a better fit than (3.10*a*,*b*) – similar to the findings in the compressible PP flow (Yao & Hussain 2020) and the cooled turbulent boundary layer (Zhang *et al.* 2018; Chen *et al.* 2022). Note that in PP flows, these relations cannot be explicitly employed to derive the mean velocity as the centreline values of mean velocity and temperature are not known *a priori*. However, such issues can be overcome for PC flows if T_c can somehow be estimated (as U_w is fixed for all cases).

Recently, an empirical scaling for T_c in compressible PP flows with symmetric isothermal boundary conditions was proposed by Song *et al.* (2022), and it can be extended to PC flows as

$$\frac{T_c}{T_w} = 1 + r_c\frac{\gamma - 1}{2}M_w^2, \tag{3.12}$$

with r_c the recovery factor for the mean temperature at the channel centreline.

Figure 12(*b*) shows the T_c/T_w as a function of M_w. It is clear that the scaling (3.12) with $r_c = 0.783$ obtained from fitting the DNS data proves to be a very good estimation

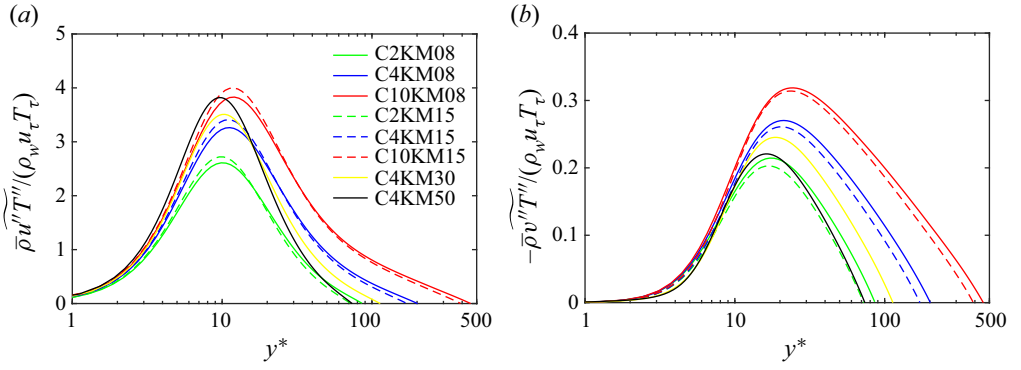

Figure 13. Streamwise $\widetilde{\bar{\rho}u''T''}/(\rho_w u_\tau T_\tau)$ and wall-normal $\widetilde{\bar{\rho}v''T''}/(\rho_w u_\tau T_\tau)$ components of turbulent heat flux as a function of y^*.

of T_c/T_w. Figure 12(*a*) further confirms that (3.11*a*,*b*) in combination with (3.12) also produces an excellent correlation between mean velocity and temperature.

The turbulent heat flux is essential for modelling compressible flows. Figure 13 shows streamwise $\widetilde{\bar{\rho}u''T''}$ and wall-normal $\widetilde{\bar{\rho}v''T''}$ components of turbulent heat flux (normalized by $\rho_w u_\tau T_\tau$) as a function of y^*. Note that the $\widetilde{\bar{\rho}v''T''}/(\rho_w u_\tau T_\tau)$ has a much smaller magnitude than $\widetilde{\bar{\rho}u''T''}/(\rho_w u_\tau T_\tau)$, and, in contrast with the Reynolds shear stress, it does not have a universal profile. For both quantities, there is a notable increase in the peak magnitude with increasing $Re^*_{\tau,c}$, and the corresponding peak location also shifts away from the wall. With increasing M_w, $\widetilde{\bar{\rho}u''T''}$ at a given Re_w increases/decreases in the near-wall/outer regions, respectively. But, $\widetilde{\bar{\rho}v''T''}$ decreases with increasing M_w in the whole range of y. Such discrepancy between different M_w cases is partially attributed to the slight difference in $Re^*_{\tau,c}$.

3.5. *Energy spectra*

Energy spectra, which illustrate how the kinetic energy of turbulence is dispersed across different scales, have been extensively utilized to get a deeper comprehension of the turbulence cascade (Jiménez 2012). Figures 14 and 15, respectively, show the premultiplied streamwise spectra $k_x E_{\rho uu}/\tau_w$ and $k_x E_{\rho uv}/\tau_w$ as a function of λ_x/h and y^*. Note that following Patel *et al.* (2015), the spectrum is computed for the velocity fluctuation weighted by the local density so that the premultiplied spectra represent its contribution to the intensity of the Reynolds stresses. It has been established previously that semilocal scaling can result in a superior collapse compared with wall unit scaling (Yao & Hussain 2019). The $k_x E_{\rho uu}/\tau_w$ spectra clearly show the presence of an energetic inner peak at $y^* \approx 13$ – corresponding to the near-wall self-sustaining regenerative cycle (Waleffe 1997; Schoppa & Hussain 2002). For a given M_w, the streamwise wavelength in physical unit λ_x/h decreases with increasing Re_τ, but remains roughly the same in semilocal units $\lambda^*_x \approx 1000$, which represents the average length of near-wall streaks. Figure 16(*a*) compares $k_x E_{\rho uu}/\tau_w$ as a function of λ^*_x between C10KM15 and I8KM00 cases. Although the length scales do not vary with M_w, the magnitudes of the inner peak increase with M_w – consistent with the larger τ_{11}/τ_w in figure 7(*a*,*b*).

Another notable difference between different M_w cases is the energy content near the channel centre. The energy at large wavelengths is enhanced with increasing M_w,

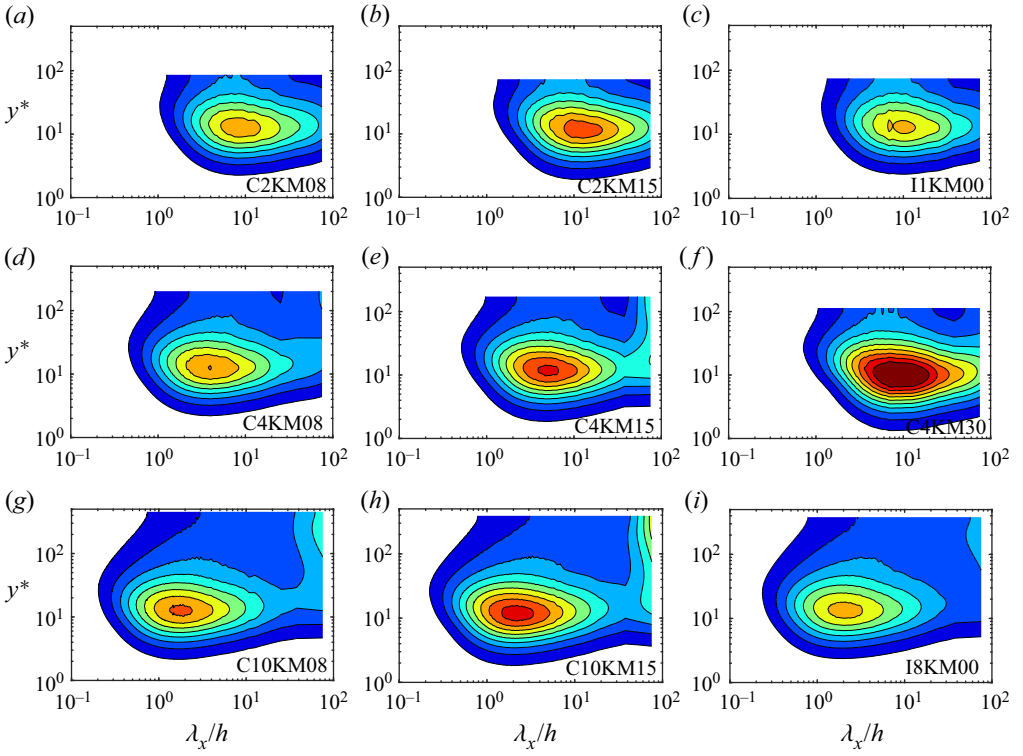

Figure 14. Premultiplied streamwise spectra of streamwise velocity $k_xE_{\rho uu}/\tau_w$.

particularly for higher $Re^*_{\tau,c}$. Note that such an increase in the energy content at large λ_x/h does not imply that the large-scale structures at high M_w are stronger than those in incompressible case but rather that they are less uniform in the streamwise direction, as depicted in the flow visualization in § 3.6. The $k_xE_{\rho uv}/\tau_w$ spectra (figure 15) have similar features to $k_xE_{\rho uu}/\tau_w$, except that the inner peak is located at smaller λ_x/h and higher y^*. In addition, the magnitude of the inner peak is less sensitive to M_w and $Re^*_{\tau,c}$ – consistent with that observed for the Reynolds shear stress τ_{12}/τ_w profiles in figure 9.

Figures 17 and 18 display the premultiplied spanwise spectra $k_zE_{\rho uu}/\tau_w$ and $k_zE_{\rho uv}/\tau_w$, respectively. First, a distinct low wavelength peak in $k_zE_{\rho uu}/\tau_w$ occurs near the wall. For both the incompressible and compressible cases, the typical length scale of the peak remains nearly universal in semilocal units, namely, $\lambda^*_z \simeq 110$. A salient feature of the PC flow is the pronounced peak at large spanwise wavelengths. This peak has its maximum magnitude at the centreline and spans almost the whole channel (i.e. until $y^* \approx 5$). It results from the large-scale streamwise rollers inherent to PC flow, whose strength increases with the Reynolds number (Komminaho *et al.* 1996; Tsukahara *et al.* 2006). Different from the $k_xE_{\rho uu}/\tau_w$, good agreements of $k_zE_{\rho uu}/\tau_w$ can be observed between the compressible and incompressible cases at comparable $Re^*_{\tau,c}$ (see figure 16*b*) – suggesting that these large-scale structures have similar features in the spanwise direction. The spanwise scale of the outer peak is approximately $\lambda_z/h \sim 1.5\pi$, which is one quarter of our spanwise domain – similar to the previous observations by Avsarkisov *et al.* (2014) and Lee & Moser (2018). In addition, for a given Re_w, the magnitude of the peak decreases with increasing M_w – consistent with a decrease in $Re^*_{\tau,c}$. Note that in the PP flow, a distinct

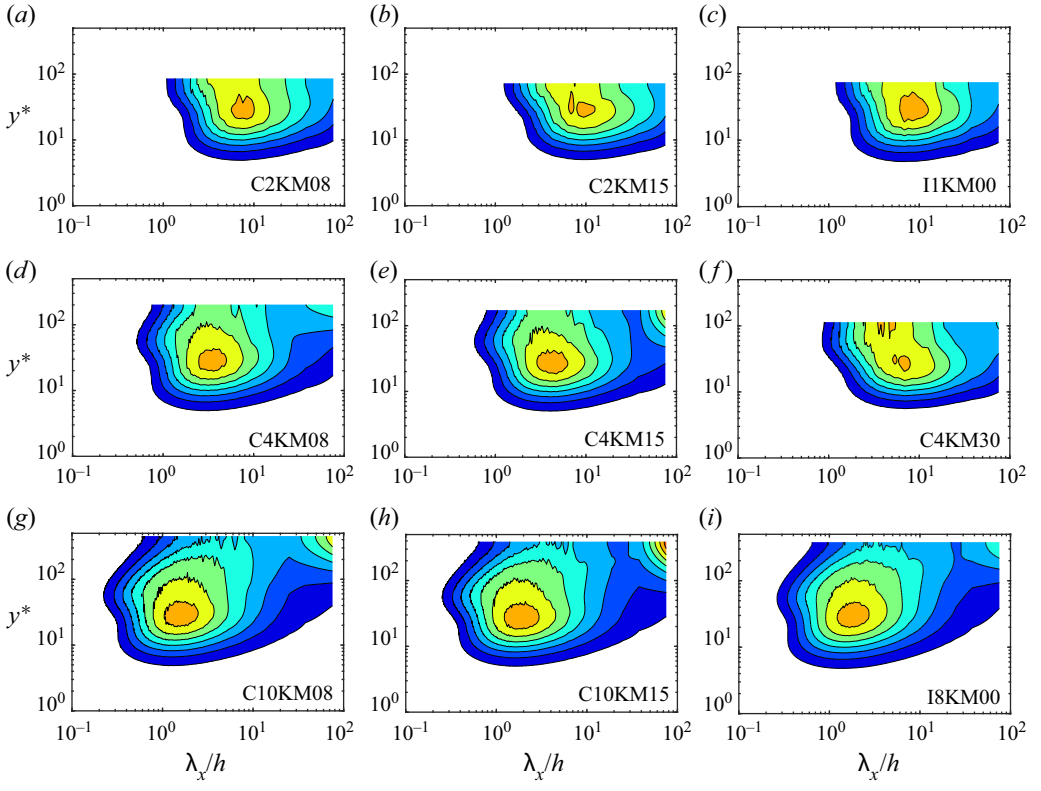

Figure 15. Premultiplied streamwise spectra of Reynolds shear stress $k_x E_{\rho uv}/\tau_w$.

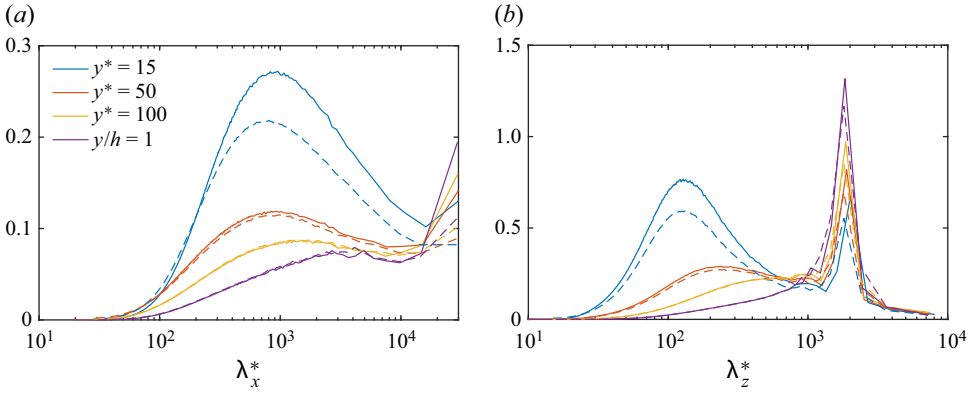

Figure 16. One-dimensional premultiplied spectra of streamwise velocity $kE_{\rho uu}/\tau_w$ at different wall-normal locations as functions of (*a*) λ_x^* and (*b*) λ_z^* for C10KM15 and I8KM00 cases.

outer peak is not observed until $Re_\tau > 5000$ (Lee & Moser 2015), and it is with a much smaller spanwise length scale (i.e. $\lambda_z \sim h$) and does not extend that close to the wall.

The $k_z E_{\rho uv}/\tau_w$ spectra are quite similar to $k_z E_{\rho uu}/\tau_w$, but the sharp peak at large spanwise wavelengths does not extend that near to the wall. The contributions of large-scale structures (defined with scales that with spanwise wavelength $\lambda_z \geq 0.5\pi h$) to

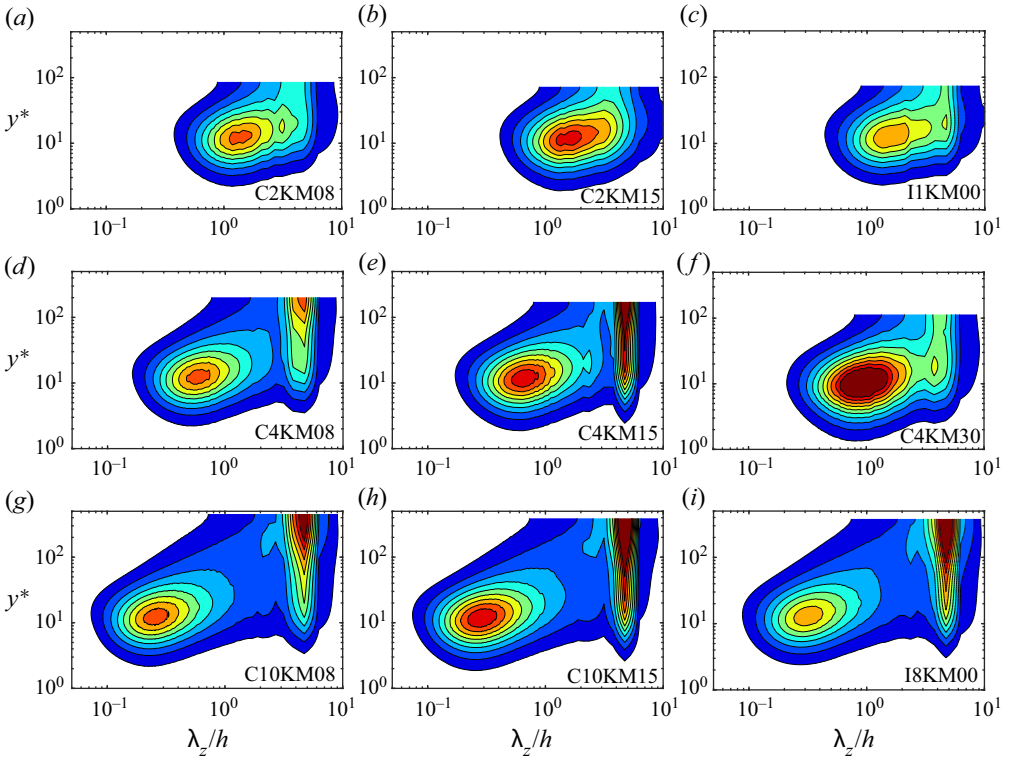

Figure 17. Premultiplied spanwise spectra of streamwise velocity $k_z E_{\rho uu}/\tau_w$.

the Reynolds stresses are further shown in figures 7 and 9 for C10KM15 and I8KM00 cases. They progressively increase with y and achieve their maximum near channel centreline (e.g. approximately 40 % of the total Reynolds shear stress at $y/h = 0$).

3.6. *Instantaneous turbulence structures*

Figure 19 visualizes the instantaneous streamwise velocity field in the x–z plane at the channel centreline (i.e. $y/h = 0$). For all cases, there are well-defined streaks that alternate in sign along the spanwise direction. For a given M_w, the streaks undergo strong meandering along the streamwise directions at low $Re^*_{\tau,c}$ and become stronger and more streamwise uniform as $Re^*_{\tau,c}$ increases (e.g. see the middle column for C2KM15, C4KM15 and C10KM15 cases). This is consistent with the finding by Lee & Moser (2018) that the coherence of the streaks significantly increases with Reynolds number, and, eventually, the large-scale meandering becomes too small to be identified even with a relatively large simulation domain (e.g. $L_x = 100\pi h$). And for a given $Re^*_{\tau,c}$ case, the streaks for the compressible cases are less organized/coherent in streamwise direction than in incompressible cases – akin to the observation by Buell (1991). For example, the streaks for the incompressible I8KM00 case become almost streamwise uniform but remain wavy for the supersonic C10KM15 case, which are responsible for the strong energy content at large wavelengths in the streamwise spectrum (figure 14). This finding is also consistent with the instability analysis by Malik, Alam & Dey (2006), who found that the most unstable streamwise wavenumber increases with M_w.

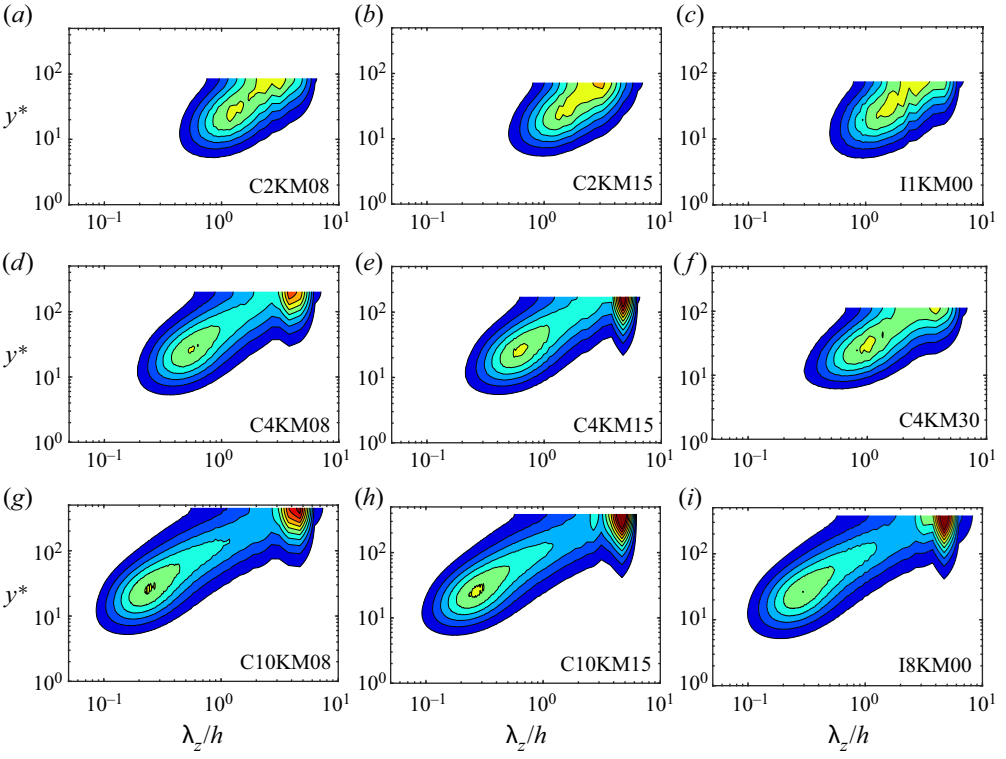

Figure 18. Premultiplied spanwise spectra of Reynolds shear stress $k_z E_{\rho uv}/\tau_w$.

Figure 20 shows a snapshot of the instantaneous streamwise velocity in a cross-stream (y–z) plane for the I8KM00 and C10KM15 cases. First, numerous small-scale streaks appear near both walls, and their sizes in the physical unit are comparable between these two cases. Furthermore, there also exist large-scale streaks, with the spanwise length scale comparable to the channel height. For the I8KM00 case, the large-scale streaks extend beyond the centreline, reaching very close to the opposite wall. This effect is less apparent for the C10KM15 case – mainly due to the density stratification caused by the wall cooling. Since the spanwise wavelength remains the same, the flank angles of the large-scale streaks become smaller for the compressible case – affecting the generation of large-scale streamwise vortices via instability/transient growth (Waleffe 1997; Schoppa & Hussain 2002).

Figure 21 further shows the vortical structures in the bottom half-channel (i.e. $-1 \leq y \leq 0$) together with the streamwise velocity fluctuations (u'/U_w) at $y^* = 15$. Note that the vortices are visualized using the isosurfaces of λ_ρ criterion (Yao & Hussain 2018). The distributions of λ_ρ structures are quite similar between the I8KM00 and C10KM15 cases. While the buffer layer is dominated by quasi-streamwise vortices, the log and outer regions exhibit a few hairpin-like vortices. Furthermore, the footprint of large-scale streaks influences the strengths of these vortical structures. Specifically, they are stronger/weaker in the vicinity of large-scale high-speed/low-speed regions, respectively – consistent with the observation of previous studies (Ganapathisubramani *et al.* 2012; Hwang & Sung 2017).

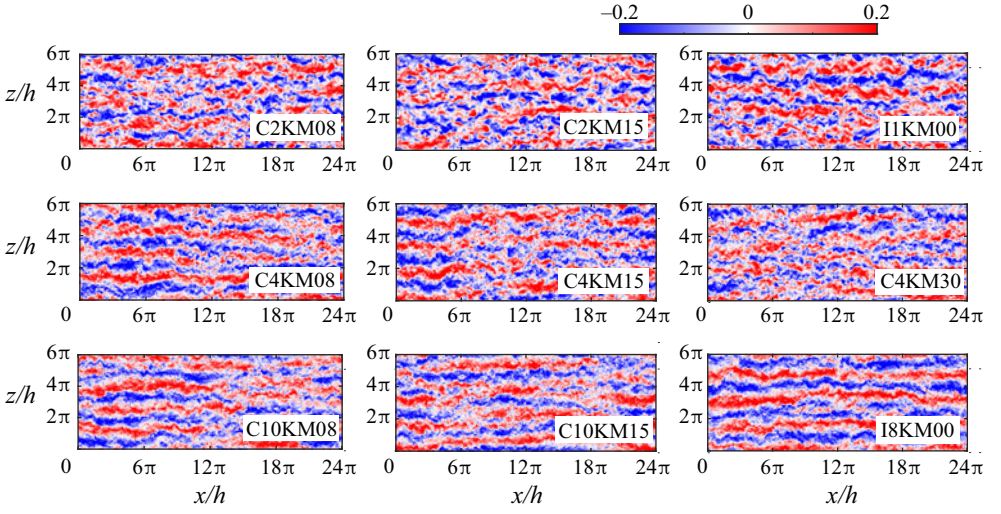

Figure 19. Instantaneous streamwise velocity in $x-z$ plane at the channel centreline (i.e. $y/h=0$).

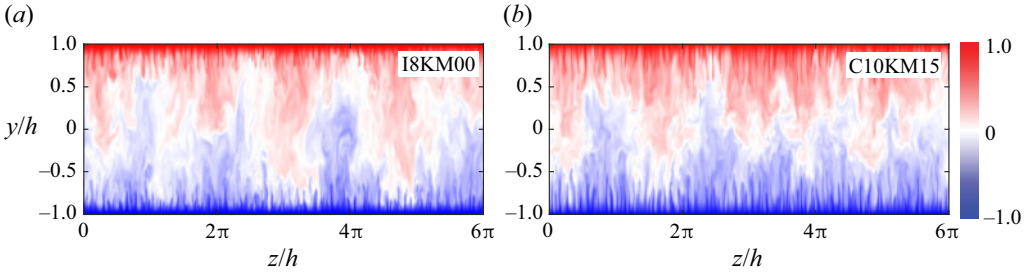

Figure 20. Comparison of instantaneous streamwise velocity in a cross-stream (y–z) plane for (a) I8KM00 and (b) C10KM15 cases.

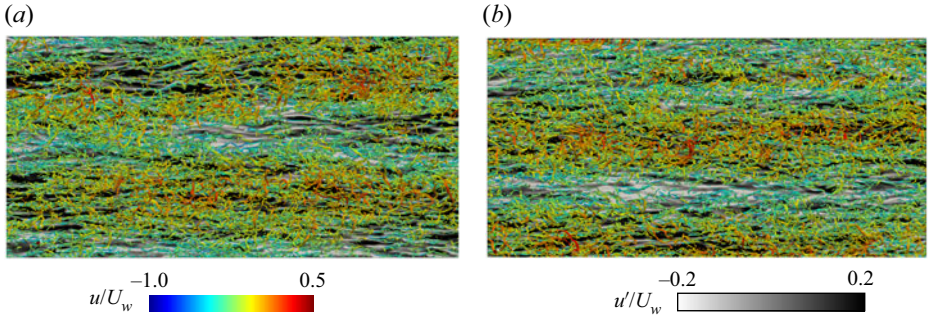

Figure 21. Instantaneous λ_ρ vortical structures shaded with the streamwise velocity u for (a) I8KM00 and (b) C10KM15 cases. Note that the grey colour denotes the streamwise velocity fluctuations u'/U_w at $y^*=15$.

3.7. *Large-scale streamwise rollers*

Considering that streamwise coherence exists throughout the entire streamwise computational domain, we further compare the time evolution of streamwise-averaged

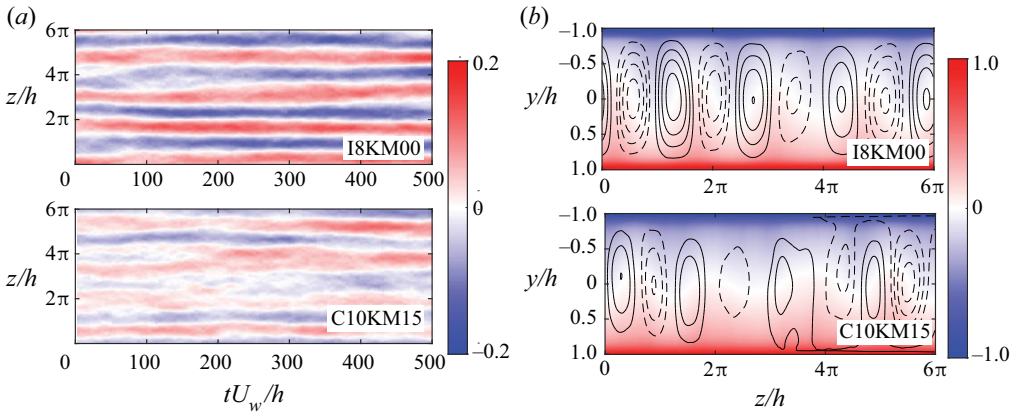

Figure 22. (*a*) Time evolution of streamwise velocity u averaged in streamwise direction at the channel centreline as a function of z; (*b*) streamwise- and temporal-averaged streamwise velocity and the streamfunction with solid and dashed lines denoting the positive and negative values, respectively.

velocity $\langle u\rangle_x$ at the channel centreline for I8KM00 and C10KM15 cases (figure 22*a*). Similar to the findings in Lee & Moser (2018), $\langle u\rangle_x$ for the I8KM00 case also appears to be coherent in time with no significant spanwise drift over time. This suggests that a more comprehensive representation of the large-scale structures can be obtained through further temporal averaging. Figure 22(*b*) shows the corresponding streamwise- and time-averaged streamwise velocity $\langle u\rangle_{x,t}$ and streamfunction in the cross-stream (y–z) plane. The structures are composed of pairs of counter-rotating streamwise rollers that occupy the entire region between the two walls. Note that due to the periodic boundary condition employed, the separation distance between these counter-rotating rollers Δz_r slightly depends on the spanwise domain size. For example, Δz_r is $L_z/4(= 1.5\pi h)$ in our case but is $\Delta z_r = 5\pi/3$ in Lee & Moser (2018). As the streamwise velocity for compressible cases is meandering in the streamwise direction, $\langle u\rangle_x$ has a relatively smaller amplitude than in incompressible cases. Furthermore, it is also less coherent in time, particularly for the C10KM15 case. Consequently, compared with the I8KM00 case, the streamwise and temporal averaged large-scale structures are less organized.

The two-point auto-correlation of the streamwise velocity is employed to probe the nature of the large-scale structures quantitatively

$$R_{uu}(r_x, r_z, y, y_r) = \frac{\langle u'(x_r, y_r, z_r)u'(x + r_x, y, z + r_z)\rangle}{\langle u'^2\rangle^{1/2}(y)\langle u'^2\rangle^{1/2}(y_r)}, \tag{3.13}$$

where (x_r, y_r, z_r) is the reference point, and r_x and r_z are the separation distances in the x- and z-directions, respectively.

Figure 23 displays the two-point auto-correlation of the streamwise velocity at the centreline $R_{uu}(r_x, r_z, 0, 0)$ for I8KM00 and C10KM15 cases. First, there is a regular alternation in the sign of $R_{uu}(r_x, r_z, 0, 0)$ in the spanwise direction, with a wavelength $\lambda_z/h = 1.5\pi$, which does not vary with M_w – consistent with the presence of the prominent peaks in the spanwise energy spectra in figure 17. As observed by Lee & Moser (2018), the correlation coefficients for the I8KM00 case do not alter the sign over the entire streamwise direction – indicating that the computational domain size employed is not sufficient for capturing one streamwise wavelength of the large-scale structures. With increasing M_w, $R_{uu}(r_x, 0, 0, 0)$ drops much faster and changes the sign for the C10KM15 case. The location for $R_{uu}(r_x, 0, 0, 0)$ to be zero becomes shorter with higher M_w.

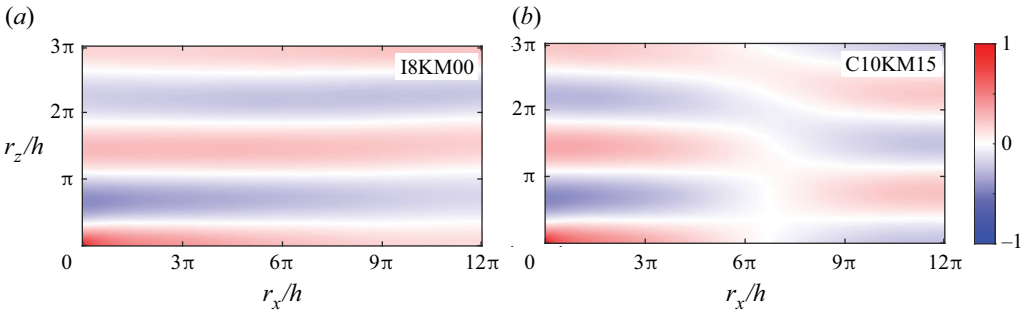

Figure 23. Two-point correlations of streamwise velocity $R_{uu}(r_x, r_z, 0, 0)$ in the x–z plane at the channel centreline.

It implies that the streamwise wavelength of the dominant large-scale structures decreases with increasing M_w. A much longer streamwise domain size would obviously be required to measure the exact length scale.

Figures 24(a) and 24(b), respectively, show the contour plots of the two-point auto-correlation of the streamwise velocity in the (x–y) and (x–z) planes for the C10KM15 case. Note that the reference point is chosen to be in the channel centre (i.e. $y_r = 0$), and the dashed lines denote the results for the I8KM00 case. Consistent with the energy spectra, the structures fill in the whole domain between the two moving walls. The distribution of $R_{uu}(r_x, 0, y, 0)$ are leading (top wall) and trailing (bottom wall) with respect to the centreline. In addition, the negative correlation appears in a wide region of $r_x > 6\pi h$. Note that the negative region is not observed for the I8KM00 case – consistent with the results shown in figure 19 that the streaks are almost streamwise uniform. The distribution of $R_{uu}(0, r_z, y, 0)$ reveals the existence of organized pairs of counter-rotating streamwise rollers, which share similar characteristics between the C10KM15 and C8KM00 cases.

3.8. *Amplitude modulation*

The modulating effect of outer large-scale streamwise rollers on the near-wall small-scale structures is further investigated here. This was first studied by Bandyopadhyay & Hussain (1984) and later extended by Mathis, Hutchins & Marusic (2009) by introducing a single-point correlation coefficient

$$R_{AM}(y^+) = \frac{\overline{u_L^+ E_L(u_S^+)}}{\sqrt{\overline{u_L^{+2}}}\sqrt{\overline{E_L(u_S^+)^2}}}, \tag{3.14}$$

where $\sqrt{\overline{u_L^{+2}}}$ and $\sqrt{\overline{E_L(u_S^+)^2}}$ denote the r.m.s. of the large-scale signal u_L^+ and the filtered envelope of small-scale signal $E_L(u_S^+)$. Note that $E_L(u_S^+)$ is obtained by applying Hilbert transform to the small-scale component u_S^+ and then low-passed filtered at the same cutoff wavelength as the large-scale component. When considering amplitude modulation, it typically requires at least information at two different wall-normal locations, hence the two-point correlations. However, Mathis *et al.* (2009) showed that the one-point correlation R_{AM} provided a fair estimation of the degree of modulation when compared with the ideal two-point coefficient. The reason is that the large scales in the outer region affect the near-wall small scales through direct penetration; hence, they have their footprint

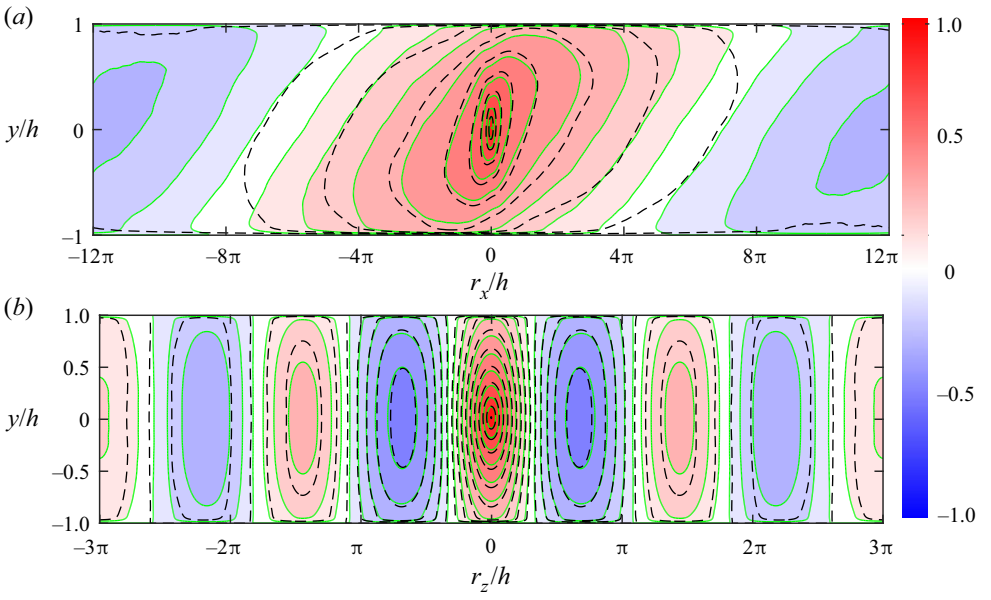

Figure 24. Two-point correlations of streamwise velocity (*a*) $R_{uu}(r_x, 0, y, 0)$ and (*b*) $R_{uu}(0, r_z, y, 0)$ for the C10KM15 case. The black dashed line is for the I8KM00 case.

in the near wall, which is evident from the premultiplied energy spectra (figure 17) and instantaneous flow visualization (figure 21).

Following Dogan *et al.* (2019), we employ the two-dimensional spectral filter to separate the velocity filed into large and small scales. In particular, the small scales are defined as those with wavelengths smaller than the cutoffs both in the streamwise and spanwise directions. Regarding the cutoffs, $\lambda_x/h \approx 2\pi$ and $\lambda_z/\delta \approx 0.5\pi$ are used, which, based on inspection of the spectra (figures 16 and 17), represent the boundary between the large and small scales. (Note that altering the filter size revealed no qualitative difference is noticed.)

Figure 25 shows the one-point amplitude modulation coefficient R_{AM} as a function of y^*. For comparison, results from PP flows at $Re_\tau = 380$ (Yao & Hussain 2020) and from turbulent boundary layer at $Re_\tau \approx 3000$ (Mathis *et al.* 2009) are also included. A large R_{AM} (i.e. 0.6) in the viscous sublayer suggests a high level of modulation of the near-wall small scales by the large scales, presumably the streamwise rollers. This effect is of major significance regarding the roles and large-scale and very-large-scale motions as their footprints interact (via both sweep and shear) with near-wall, small-scale structures. The value of R_{AM} decreases to approximately zero in the log region and becomes negative in the outer region. Furthermore, R_{AM} between the I8KM00 and C10KM15 cases collapse very well across the whole wall-normal range. This shows that the modulation effect between incompressible and compressible cases is quite similar when the semilocal Reynolds numbers at the channel centreline $Re^*_{\tau,c}$ are equal. In addition, R_{AM} in PC flows is much stronger than in PP flows at comparable Re_τ and is nearly comparable to turbulent boundary layer at much higher Re_τ (i.e. ≈ 3000). Therefore, PC flow can be employed to better explore the physics and control of the large- and small-scale interactions – without the need for extremely high Reynolds numbers (Pirozzoli, Bernardini & Orlandi 2011).

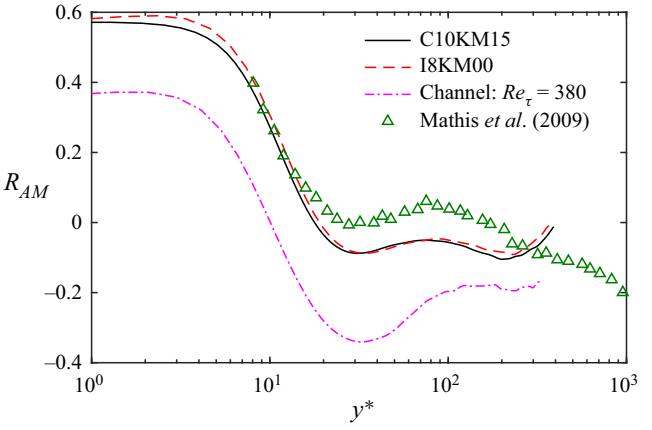

Figure 25. Distribution of the one-point amplitude modulation coefficient R_{AM} for C10KM15 and I8KM00 cases.

4. Concluding remarks

Direct numerical simulations of compressible turbulent PC flows are conducted for $Re_w = 1500$, 4000 and 10 000 with the highest M_w up to 5. While C_f decreases with Re_w, it only weakly depends on M_w. In addition, the thermodynamic properties (e.g. mean temperature, density, etc.) strongly vary with M_w. Consistent with prior research on other types of wall turbulence, the compressibility effects on most turbulent statistics can be well incorporated by using the semilocal scaling based on the local mean viscosity and density. In particular, the mean velocity profiles under TL transformation (Trettel & Larsson 2016) collapse very well with the incompressible ones at comparable $Re^*_{\tau,c}$ and develop a logarithmic layer that extends closer to the channel centreline with a Kárman constant $\kappa = 0.41$. Reynolds stresses exhibit the same behaviours as incompressible flows, including peak locations and magnitudes. The inner peak of the streamwise Reynolds stress for PC increases with M_w, which is consistent with the findings for compressible PP flows. In addition, due to rapid wall-normal changes of viscosity caused by viscous heating, the turbulent production in the near-wall region decreases as M_w increases, and its peak, when scaled in wall units, follows $P^+_k(y^*_P) = (\mu_w/\mu(y^*_P))/4$, where $y^*_P(\approx 11)$ is the peak location in semilocal units.

The one-dimensional streamwise and spanwise premultiplied velocity spectra are also examined. The streamwise velocity spectra show a distinct inner peak located at $\lambda^*_x \approx 1000$ and $\lambda^*_z \approx 110$ – indicating that the near-wall structures are universal for all types of wall turbulence. In addition, the spanwise spectra display an outer peak located at $\lambda_z/h \approx 1.5h$. This peak has its maximum magnitude at the centreline and spans over the whole channel depth (i.e. until approximately $y^* = 5$) – resulting from the large-scale streamwise structures specific to PC flows. The characteristics of these structures are examined by flow visualization. For strictly incompressible cases, the structures are comprised pairs of streamwise-uniform, counter-rotating rollers that occupy the entire region between the two parallel walls. As M_w increases, the large-scale structures become less organized/coherent in the streamwise direction. The two-point auto-correlation further confirms that the streamwise length scale of these structures decreases with increasing M_w. The reason for this still needs further investigation. The amplitude modulation of near-wall small-scale structures by the large-scale streamwise rollers is also studied. A high level of modulation of large scales on small scales is observed close to the wall. In addition, the modulation

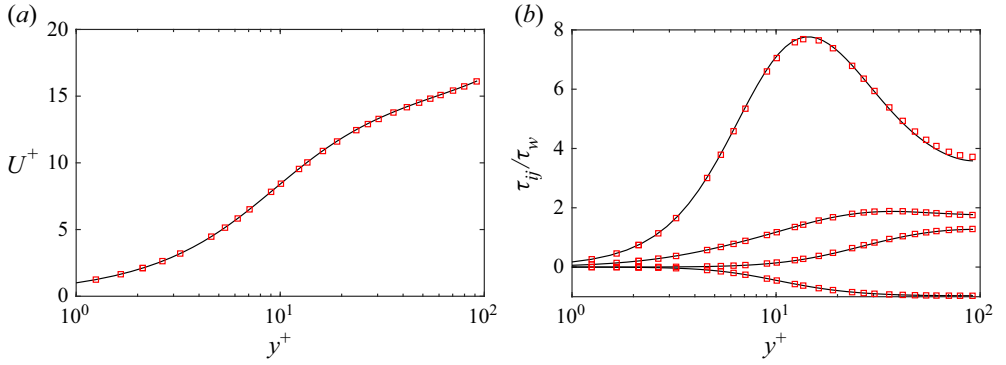

Figure 26. (*a*) Mean velocity (U^+) and (*b*) velocity variances and covariance for the case with $Re_w = 1500$ and $M_w = 0.2$. Solid lines and circles, respectively, represent results from our DNS and from Lee & Moser (2018) at $Re_\tau = 93$.

effect is quite similar between incompressible and compressible cases at similar $Re^*_{\tau,c}$ – but much stronger than in PP flows.

Acknowledgements. We appreciate M. Lee and R. Moser for providing us with their incompressible DNS code used for this study.

Funding. Computational and visualization resources provided by Texas Tech University HPCC, TACC Lonestar, Stampede2 and Frontera are acknowledged.

Declaration of interests. The authors report no conflict of interest.

Data availability statement. The data that support the findings of this study are openly available at https://dataverse.tdl.org/dataverse/ctpcf.

Author ORCIDs.
Jie Yao https://orcid.org/0000-0001-6069-6570;
Fazle Hussain https://orcid.org/0000-0002-2209-9270.

Appendix A. Validation of numerical solver for PC flow at low Mach number

The solver has been extensively validated in our previous works (Yao & Hussain 2019, 2020) for the PP configuration by comparing flow statistics with both the incompressible dataset of Lee & Moser (2015) and the compressible dataset of Modesti & Pirozzoli (2016). The solver is validated here for the compressible PC flow at $Re_w = 1500$ in the nearly incompressible region (i.e. $M_w = 0.2$) and compared with the strictly incompressible data of Lee & Moser (2018). The domain size and the corresponding number of grid points are the same as in the C2KM08 and C2KM15 cases, which results in mesh resolutions of $\Delta x^+ = 9.2$, $\Delta y^+_w = 0.22$, $\Delta y^+_c = 2.99$ and $\Delta z^+ = 4.6$. Figure 26 shows the profiles of mean velocity (U^+) and Reynolds stresses (τ^+_{ij}). Excellent agreement is observed, except for minor differences near the peak and centre of τ^+_{11}.

Appendix B. Domain size effect for compressible PC flow

Numerical simulations of PC flow with periodic boundary conditions are known to be highly sensitive to the computational domain size – potentially leading to artificial confinement effects (Komminaho *et al.* 1996; Pirozzoli *et al.* 2014). The effect of the domain size on flow physics is further examined by performing additional DNSs with

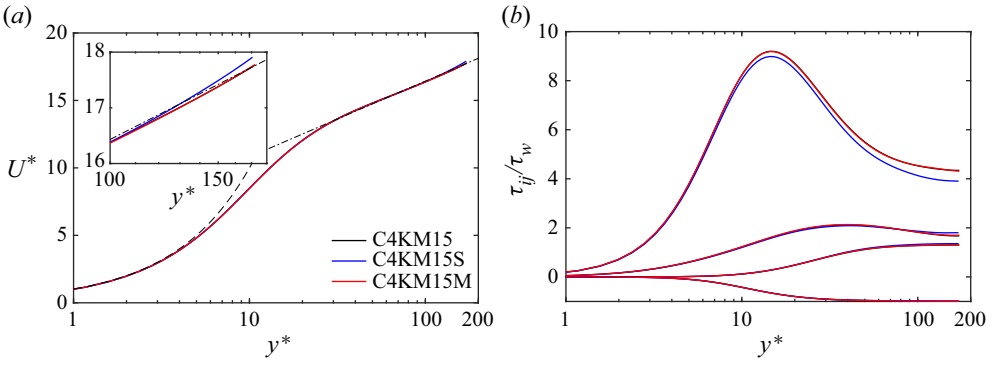

Figure 27. (*a*) The TL transformed mean velocity profiles transformed and (*b*) Reynolds stresses for different domain sizes with $Re_w = 4000$ and $M_w = 1.5$. The dashed and dash-dotted lines in (*a*) denote $U^* = y^*$ and log law $U^* = (1/\kappa)\ln y^* + B$, where $\kappa = 0.41$ and $B = 5.2$.

Case	Re_τ	$Re^*_{\tau,c}$	$L_x \times L_y \times L_z$	$N_x \times N_y \times N_z$	Tu_τ/h	ψ
C4KM15S	249.4	170.6	$12\pi h \times 2h \times 3\pi h$	$768 \times 193 \times 384$	48.3	0.190
C4KM15M	251.5	172.2	$24\pi h \times 2h \times 3\pi h$	$1536 \times 193 \times 384$	32.7	0.167

Table 4. Summary of the simulation parameters for different domain size cases with $Re_w = 4000$ and $M_w = 1.5$. Here, ψ is the velocity gradient at the channel centreline.

various streamwise and spanwise lengths at $Re_w = 4000$ and $M_w = 1.5$. The details of domain sizes, grid sizes and resolutions are listed in table 4.

Figure 27(*a*) shows the mean velocity profiles based on the TL transformation as a function of y^*. While the agreement between different cases is good in the near-wall region, notable discrepancies are observed near the channel centreline. Compared with the C4KM15 case, the velocity gradient at the channel centreline ψ for the C4KM15S case is increased by approximately 16 % (table 4). This suggests that the larger discrepancy in ψ results from the domain size effect, particularly in the streamwise direction. Figure 27(*b*) shows the Reynolds normal and shear stresses as a function of y^*. Interestingly, τ_{11}/τ_w is the only component that exhibits certain disagreement. Specifically, τ_{11}/τ_w for the C4KM15S case is slightly smaller than in other cases, particularly in the outer regions. It confirms that the domain size employed in the main text is sufficient to yield good statistics. Figure 28 shows the two-point auto-correlation of the streamwise velocity at the centreline $R_{uu}(r_x, r_z, 0, 0)$ for different domain size cases. Consistent with figure 23, a regular alternation in the sign of $R_{uu}(r_x, r_z, 0, 0)$ in the spanwise direction exists, and the wavelength is the same between different cases; namely, $\lambda_z/h = 1.5\pi$. This confirms that the characteristics of the large-scale spanwise roller is not very sensitive to the spanwise domain size. The correlation coefficients for the C4KM15S case do not alter sign across the entire streamwise direction. In particular, the correlation falls to 0.15 at $r_x/h = L_x/2$ and $r_z = 0$ – indicating that the streamwise computational domain size (i.e. $L_x = 12\pi$) is not sufficient for capturing one streamwise wavelength of the large-scale structures. With increasing L_x, $R_{uu}(r_x, 0, 0, 0)$ does change sign. It is approximately $r_x/h \approx 6\pi$ for the C4KM15M case – consistent with the observation in figure 23 for the C10KM15 case.

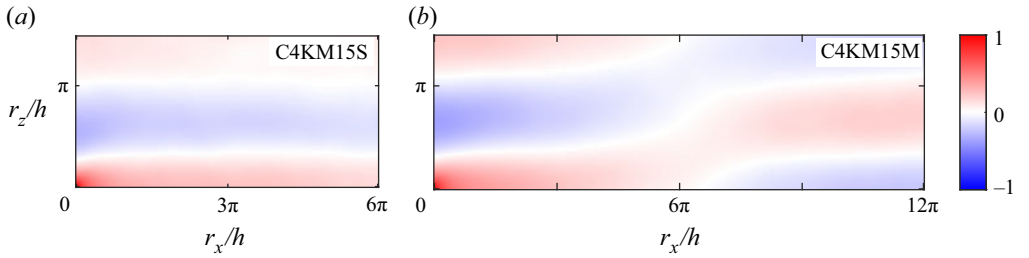

Figure 28. Two-point correlations of streamwise velocity $R_{uu}(r_x, r_z, 0, 0)$ in a wall-parallel (x–z) plane at the channel centreline for different domain sizes with $Re_w = 4000$ and $M_w = 1.5$.

References

Avsarkisov, V., Hoyas, S., Oberlack, M. & Garcia-Galache, J.P. 2014 Turbulent plane couette flow at moderately high Reynolds number. *J. Fluid Mech.* **751**, R1.

Bandyopadhyay, P.R. & Hussain, A.K.M.F. 1984 The coupling between scales in shear flows. *Phys. Fluids* **27** (9), 2221–2228.

Baranwal, A., Donzis, D.A. & Bowersox, R.D.W. 2022 Asymptotic behaviour at the wall in compressible turbulent channels. *J. Fluid Mech.* **933**, A28.

Buell, J.C. 1991 Direct simulations of compressible wall-bounded turbulence. *Annual Research Briefs-1990*, p. 347. Center for Turbulence Research.

Busse, F.H. 1970 Bounds for turbulent shear flow. *J. Fluid Mech.* **41** (1), 219–240.

Chagelishvili, G.D., Rogava, A.D. & Segal, I.N. 1994 Hydrodynamic stability of compressible plane Couette flow. *Phys. Rev.* E **50** (6), R4283.

Chen, P.E.S., Lv, Y., Xu, H.H.A., Shi, Y. & Yang, X.I.A. 2022 Les wall modeling for heat transfer at high speeds. *Phys. Rev. Fluids* **7** (1), 014608.

Chen, X. & Sreenivasan, K.R. 2021 Reynolds number scaling of the peak turbulence intensity in wall flows. *J. Fluid Mech.* **908**, R3.

Cheng, W., Pullin, D.I. & Samtaney, R. 2022 Wall-resolved and wall-modelled large-eddy simulation of plane Couette flow. *J. Fluid Mech.* **934**, A19.

Dawson, S.T. & McKeon, B.J. 2019 Studying the effects of compressibility in planar Couette flow using resolvent analysis. In *AIAA Scitech 2019 Forum*, p. 2139. AIAA.

Dogan, E., Örlü, R., Gatti, D., Vinuesa, R. & Schlatter, P. 2019 Quantification of amplitude modulation in wall-bounded turbulence. *Fluid Dyn. Res.* **51** (1), 011408.

Driest, E.R.V. 1951 Turbulent boundary layer in compressible fluids. *J. Aeronaut. Sci.* **18** (3), 145–160.

Duan, L., Beekman, I. & Martin, M.P. 2010 Direct numerical simulation of hypersonic turbulent boundary layers. Part 2. Effect of wall temperature. *J. Fluid Mech.* **655**, 419–445.

Duan, L., Beekman, I. & Martin, M.P. 2011 Direct numerical simulation of hypersonic turbulent boundary layers. Part 3. Effect of mach number. *J. Fluid Mech.* **672**, 245–267.

Duck, P.W., Erlebacher, G. & Hussaini, M.Y. 1994 On the linear stability of compressible plane Couette flow. *J. Fluid Mech.* **258**, 131–165.

El Telbany, M.M.M. & Reynolds, A.J. 1982 The structure of turbulent plane Couette flow. *J. Fluids Engng* **104** (3), 367–372.

Foysi, H., Sarkar, S. & Friedrich, R. 2004 Compressibility effects and turbulence scalings in supersonic channel flow. *J. Fluid Mech.* **509**, 207–216.

Fukagata, K., Iwamoto, K. & Kasagi, N. 2002 Contribution of Reynolds stress distribution to the skin friction in wall-bounded flows. *Phys. Fluids (1994-present)* **14** (11), L73–L76.

Ganapathisubramani, B., Hutchins, N., Monty, J.P., Chung, D. & Marusic, I. 2012 Amplitude and frequency modulation in wall turbulence. *J. Fluid Mech.* **712**, 61–91.

Ghosh, S., Foysi, H. & Friedrich, R. 2010 Compressible turbulent channel and pipe flow: similarities and differences. *J. Fluid Mech.* **648**, 155–181.

Griffin, K.P., Fu, L. & Moin, P. 2021 Velocity transformation for compressible wall-bounded turbulent flows with and without heat transfer. *Proc. Natl Acad. Sci.* **118** (34), e2111144118.

Hadjadj, A., Ben-Nasr, O., Shadloo, M.S. & Chaudhuri, A. 2015 Effect of wall temperature in supersonic turbulent boundary layers: a numerical study. *Intl J. Heat Mass Transfer* **81**, 426–438.

HOYAS, S., OBERLACK, M., ALCÁNTARA-ÁVILA, F., KRAHEBERGER, S.V. & LAUX, J. 2022 Wall turbulence at high friction Reynolds numbers. *Phys. Rev. Fluids* **7** (1), 014602.

HU, S. & ZHONG, X. 1998 Linear stability of viscous supersonic plane Couette flow. *Phys. Fluids* **10** (3), 709–729.

HUANG, P.G., COLEMAN, G.N. & BRADSHAW, P. 1995 Compressible turbulent channel flows: DNS results and modelling. *J. Fluid Mech.* **305**, 185–218.

HUANG, J., DUAN, L. & CHOUDHARI, M.M. 2022 Direct numerical simulation of hypersonic turbulent boundary layers: effect of spatial evolution and Reynolds number. *J. Fluid Mech.* **937**, A3.

HWANG, J. & SUNG, H.J. 2017 Influence of large-scale motions on the frictional drag in a turbulent boundary layer. *J. Fluid Mech.* **829**, 751–779.

JIMÉNEZ, J. 2012 Cascades in wall-bounded turbulence. *Annu. Rev. Fluid Mech.* **44**, 27–45.

KIM, J., MOIN, P. & MOSER, R. 1987 Turbulence statistics in fully developed channel flow at low Reynolds number. *J. Fluid Mech.* **177**, 133–166.

KITOH, O., NAKABYASHI, K. & NISHIMURA, F. 2005 Experimental study on mean velocity and turbulence characteristics of plane couette flow: low-Reynolds-number effects and large longitudinal vortical structure. *J. Fluid Mech.* **539**, 199–227.

KOMMINAHO, J., LUNDBLADH, A. & JOHANSSON, A.V. 1996 Very large structures in plane turbulent Couette flow. *J. Fluid Mech.* **320**, 259–285.

LEE, M.J. & KIM, J. 1991 The structure of turbulence in a simulated plane Couette flow. In *Proceedings of the 8th Symposium on Turbulent Shear Flow, Technical University of Munich, Germany*, vol. 5.

LEE, M. & MOSER, R.D. 2015 Direct numerical simulation of turbulent channel flow up to Re 5200. *J. Fluid Mech.* **774**, 395–415.

LEE, M. & MOSER, R.D. 2018 Extreme-scale motions in turbulent plane Couette flows. *J. Fluid Mech.* **842**, 128–145.

LI, W., FAN, Y., MODESTI, D. & CHENG, C. 2019 Decomposition of the mean skin-friction drag in compressible turbulent channel flows. *J. Fluid Mech.* **875**, 101–123.

LI, X.-L., FU, D.-X., MA, Y.-W. & LIANG, X. 2010 Direct numerical simulation of compressible turbulent flows. *Acta Mechanica Sin.* **26** (6), 795–806.

LOZANO-DURÁN, A. & JIMÉNEZ, J. 2014 Effect of the computational domain on direct simulations of turbulent channels up to re $\tau = 4200$. *Phys. Fluids* **26** (1), 011702.

LUND, K.O. & BUSH, W.B. 1980 Asymptotic analysis of plane turbulent Couette-Poiseuille flows. *J. Fluid Mech.* **96** (1), 81–104.

MALIK, M., ALAM, M. & DEY, J. 2006 Nonmodal energy growth and optimal perturbations in compressible plane Couette flow. *Phys. Fluids* **18** (3), 034103.

MALIK, M., DEY, J. & ALAM, M. 2008 Linear stability, transient energy growth, and the role of viscosity stratification in compressible plane Couette flow. *Phys. Rev.* E **77** (3), 036322.

MARUSIC, I., BAARS, W.J. & HUTCHINS, N. 2017 Scaling of the streamwise turbulence intensity in the context of inner-outer interactions in wall turbulence. *Phys. Rev. Fluids* **2** (10), 100502.

MARUSIC, I., MCKEON, B.J., MONKEWITZ, P.A., NAGIB, H.M., SMITS, A.J. & SREENIVASAN, K.R. 2010 Wall-bounded turbulent flows at high Reynolds numbers: recent advances and key issues. *Phys. Fluids* **22** (6), 065103.

MARUSIC, I. & MONTY, J.P. 2019 Attached eddy model of wall turbulence. *Annu. Rev. Fluid Mech.* **51**, 49–74.

MATHIS, R., HUTCHINS, N. & MARUSIC, I. 2009 Large-scale amplitude modulation of the small-scale structures in turbulent boundary layers. *J. Fluid Mech.* **628**, 311–337.

MODESTI, D. & PIROZZOLI, S. 2016 Reynolds and mach number effects in compressible turbulent channel flow. *Intl J. Heat Fluid Flow* **59**, 33–49.

OLIVER, T.A., MALAYA, N., ULERICH, R. & MOSER, R.D. 2014 Estimating uncertainties in statistics computed from direct numerical simulation. *Phys. Fluids* **26** (3), 035101.

PATEL, A., BOERSMA, B.J. & PECNIK, R. 2016 The influence of near-wall density and viscosity gradients on turbulence in channel flows. *J. Fluid Mech.* **809**, 793–820.

PATEL, A., PEETERS, J.W.R., BOERSMA, B.J. & PECNIK, R. 2015 Semi-local scaling and turbulence modulation in variable property turbulent channel flows. *Phys. Fluids* **27** (9), 095101.

PIROZZOLI, S. & BERNARDINI, M. 2011 Turbulence in supersonic boundary layers at moderate Reynolds number. *J. Fluid Mech.* **688**, 120–168.

PIROZZOLI, S., BERNARDINI, M. & ORLANDI, P. 2011 Large-scale motions and inner/outer layer interactions in turbulent Couette–Poiseuille flows. *J. Fluid Mech.* **680**, 534–563.

PIROZZOLI, S., BERNARDINI, M. & ORLANDI, P. 2014 Turbulence statistics in couette flow at high Reynolds number. *J. Fluid Mech.* **758**, 327–343.

PIROZZOLI, S., GRASSO, F. & GATSKI, T.B. 2004 Direct numerical simulation and analysis of a spatially evolving supersonic turbulent boundary layer at $m = 2.25$. *Phys. Fluids* **16** (3), 530–545.

PIROZZOLI, S., ROMERO, J., FATICA, M., VERZICCO, R. & ORLANDI, P. 2021 One-point statistics for turbulent pipe flow up to $re_\tau \approx 6000$. *J. Fluid Mech.* **926**, A28.

RAMACHANDRAN, A., SAIKIA, B., SINHA, K. & GOVINDARAJAN, R. 2016 Effect of prandtl number on the linear stability of compressible Couette flow. *Intl J. Heat Fluid Flow* **61**, 553–561.

REICHARDT, H. 1959 Cesetzmassigkeiten der geradlinigen turbulenten couettestromung. In *Max Plank Institute fur Stromungs forschung, Mitteilung*, vol. 22.

RENARD, N. & DECK, S. 2016 A theoretical decomposition of mean skin friction generation into physical phenomena across the boundary layer. *J. Fluid Mech.* **790**, 339–367.

REZAEIRAVESH, S., XAVIER, D., VINUESA, R., YAO, J., HUSSAIN, F. & SCHLATTER, P. 2022 Estimating uncertainty of low- and high-order turbulence statistics in wall turbulence. In *12th International Symposium on Turbulence and Shear Flow Phenomena (TSFP12) Osaka, Japan*. Available at: http://www.tsfp-conference.org/proceedings/2022/417.pdf.

ROBERTSON, J.M. & JOHNSON, H.F. 1970 Turbulence structure in plane couette flow. *J. Engng Mech. Div.* **96** (6), 1171–1182.

SCHLATTER, P. & ÖRLÜ, R. 2010 Assessment of direct numerical simulation data of turbulent boundary layers. *J. Fluid Mech.* **659**, 116–126.

SCHOPPA, W. & HUSSAIN, F. 2002 Coherent structure generation in near-wall turbulence. *J. Fluid Mech.* **453**, 57–108.

SONG, Y., ZHANG, P., LIU, Y. & XIA, Z. 2022 Central mean temperature scaling in compressible turbulent channel flows with symmetric isothermal boundaries. *Phys. Rev. Fluids* **7** (4), 044606.

SZEMBERG O'CONNOR, T. 2018 Bulk viscosity effects in compressible turbulent Couette flow. PhD thesis, Imperial College London.

TRETTEL, A. & LARSSON, J. 2016 Mean velocity scaling for compressible wall turbulence with heat transfer. *Phys. Fluids* **28** (2), 026102.

TSUKAHARA, T., KAWAMURA, H. & SHINGAI, K. 2006 Dns of turbulent couette flow with emphasis on the large-scale structure in the core region. *J. Turbul.* **7**, N19.

WALEFFE, F. 1997 On a self-sustaining process in shear flows. *Phys. Fluids* **9** (4), 883–900.

WALZ, A. 1969 *Boundary Layers of Flow and Temperature*. MIT Press.

WU, X., BALTZER, J.R. & ADRIAN, R.J. 2012 Direct numerical simulation of a 30r long turbulent pipe flow at r+= 685: large-and very large-scale motions. *J. Fluid Mech.* **698**, 235–281.

YAO, J., CHEN, X. & HUSSAIN, F. 2019 Reynolds number effect on drag control via spanwise wall oscillation in turbulent channel flows. *Phys. Fluids* **31** (8), 085108.

YAO, J., CHEN, X. & HUSSAIN, F. 2022 Direct numerical simulation of turbulent open channel flows at moderately high Reynolds numbers. *J. Fluid Mech.* **953**, A19.

YAO, J. & HUSSAIN, F. 2018 Toward vortex identification based on local pressure-minimum criterion in compressible and variable density flows. *J. Fluid Mech.* **850**, 5–17.

YAO, J. & HUSSAIN, F. 2019 Supersonic turbulent boundary layer drag control using spanwise wall oscillation. *J. Fluid Mech.* **880**, 388–429.

YAO, J. & HUSSAIN, F. 2020 Turbulence statistics and coherent structures in compressible channel flow. *Phys. Rev. Fluids* **5** (8), 084603.

YAO, J., REZAEIRAVESH, S., SCHLATTER, P. & HUSSAIN, F. 2023 Direct numerical simulations of turbulent pipe flow up to $re_\tau \approx 5200$. *J. Fluid Mech.* **956**, A18.

ZHANG, Y.-S., BI, W.-T., HUSSAIN, F. & SHE, Z.-S. 2014 A generalized Reynolds analogy for compressible wall-bounded turbulent flows. *J. Fluid Mech.* **739**, 392–420.

ZHANG, C., DUAN, L. & CHOUDHARI, M.M. 2018 Direct numerical simulation database for supersonic and hypersonic turbulent boundary layers. *AIAA J.* **56** (11), 4297–4311.